J. Fluid Mech. (2022), *vol*. 950, A9, doi:10.1017/jfm.2022.790

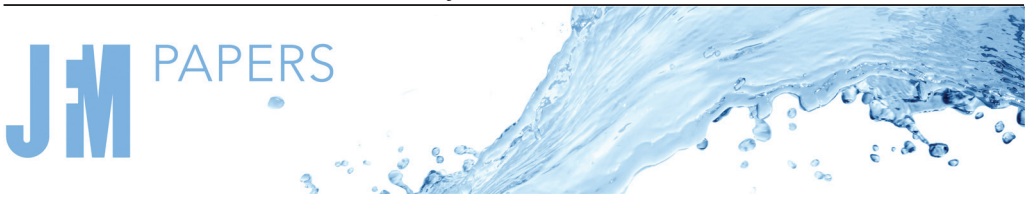

Improved convergence of the spectral proper orthogonal decomposition through time shifting

Diego C.P. Blanco[1,†], **Eduardo Martini**[2], **Kenzo Sasaki**[1] and **André V.G. Cavalieri**[1]

[1]Divisão de Engenharia Aeroespacial, Instituto Tecnológico de Aeronáutica, 12228-900 São José dos Campos/SP, Brazil

[2]Département Fluides, Thermique et Combustion, Institut Pprime, CNRS, Université de Poitiers, ENSMA, 86000 Poitiers, France

(Received 8 October 2021; revised 21 July 2022; accepted 10 September 2022)

Spectral proper orthogonal decomposition (SPOD) is an increasingly popular modal analysis method in the field of fluid dynamics due to its specific properties: a linear system forced with white noise should have SPOD modes identical to response modes from resolvent analysis. The SPOD, coupled with the Welch method for spectral estimation, may require long time-resolved datasets. In this work, a linearised Ginzburg–Landau model is considered in order to study the method's convergence. Spectral proper orthogonal decomposition modes of the white-noise forced equation are computed and compared with corresponding response resolvent modes. The quantified error is shown to be related to the time length of Welch blocks (spectral window size) normalised by a convective time. Subsequently, an algorithm based on a temporal data shift is devised to further improve SPOD convergence and is applied to the Ginzburg–Landau system. Next, its efficacy is demonstrated in a numerical database of a boundary layer subject to bypass transition. The proposed approach achieves substantial improvement in mode convergence with smaller spectral window sizes with respect to the standard method. Furthermore, SPOD modes display growing wall-normal and spanwise velocity components along the streamwise direction, a feature which had not yet been observed and is also predicted by a global resolvent calculation. The shifting algorithm for the SPOD opens the possibility for using the method on datasets with time series of moderate duration, often produced by large simulations.

Key words: low-dimensional models, turbulence modelling

† Email address for correspondence: diegodcpb@ita.br

1. Introduction

Modal analysis is a well-known method to study systems of partial differential equations (PDEs). By studying characteristics of a dynamic system, one can compute a basis in the PDE solution space and, thus, identify the underlying coherent structures governing the system's evolution in time and space. For instance, it is a established technique to develop reduced-order models (ROMs) of complex flows (Rowley & Dawnson 2017; Taira *et al.* 2020).

In the context of dynamical systems, a popular method is proper orthogonal decomposition (POD), also called principal component analysis or Karhunen–Loève decomposition in other disciplines. Introduced to the fluid dynamics community by Lumley (1967, 1970), the statistical method decomposes an ensemble of bounded signals into orthogonal deterministic modes (often called empirical eigenfunctions) which, within all possible linear decompositions, are optimal in containing the most energy in an average sense (Berkooz, Holmes & Lumley 1993).

The POD method enables the decomposition of velocity correlations from statistically stationary flows into modes, in order to identify and analyse the most energetic structures evolving in space and time. Due to its generality and solid foundation in the statistics theory, POD has been applied to numerous fluid dynamics fields, with studies involving coherent structures in turbulence (Sirovich 1987), derivations of ROMs (Ravindran 2000; Noack *et al.* 2003), among many other applications. The method gained special traction in the 1990s with the rapid development of numerical analysis and computational tools (Aubry 1991).

For statistically stationary flows, the application of POD over the Fourier transform in time of measured correlations generates modes that develop in a single frequency and display coherence in both space and time. This approach has been applied throughout the years to study jets (Glauser & George 1987; Delville *et al.* 1999; Picard & Delville 2000; Jung, Gamard & George 2004; Iqbal & Thomas 2007; Tinney & Jordan 2008; Gudmundsson & Colonius 2011; Schmidt *et al.* 2017), mixing layers (Arndt, Long & Glauser 1997; Bonnet *et al.* 1998; Citriniti & George 2000), turbulent pipes (Hellström & Smits 2014), boundary layers (Tutkun & George 2017) and wakes (Araya, Colonius & Dabiri 2017).

This form of POD in the frequency domain has been labelled spectral POD, or SPOD (Towne, Schmidt & Colonius 2018; Schmidt & Colonius 2020). It should be noted that we do not refer here to the homonym work of Sieber, Paschereit & Oberleithner (2016), which deals with a different algorithm. Towne *et al.* (2018) established an important link between statistics and dynamical systems in the frequency space, as a linear set of equations, forced with an uncorrelated (spatially white) noise in a given frequency must have SPOD modes identical to the modes obtained via resolvent analysis. This property is not always present in the form of POD, which yields purely spatial modes modulated by time-dependent coefficients, hereby called spatial POD.

Later works employing SPOD include: the development of data-driven ROMs for boundary layer transition control (Sasaki *et al.* 2020), characterisation of noise generated over airfoils (Sano *et al.* 2019; Abreu *et al.* 2021) and the identification of coherent structures in channels (Abreu *et al.* 2020*a*), wakes (Nidhan *et al.* 2020; Li *et al.* 2021), separated high-speed flows (Lugrin *et al.* 2021) and complex geometries (Zhang, Ooka & Kikumoto 2021; He *et al.* 2021).

Despite its versatility, the proposed SPOD algorithm (Towne *et al.* 2018) leads to some inherent complexity related to spectral estimation. It relies on the Welch method (Welch 1967) for the estimation of the cross-spectral density (CSD) tensor, and hence,

computed gains and modes are sensitive to sampling parameters (number of field snapshots/realisations N_t, time step δt) and estimation parameters (number of blocks, N_b, number of snapshots per block, N_{FFT}, windowing function, $w(t)$, and overlap between successive blocks, O_{FFT}). For a given dataset with N_t snapshots separated by a constant time step δt, increasing N_b implies decreasing N_{FFT} and *vice versa*. A larger N_b penalises frequency resolution, increases spectral leakage and may lead to results contaminated with statistical bias, whereas a larger N_{FFT} penalises convergence by decreasing the number of averaging blocks. The appropriate compromise between these cases is problem dependent and literature concerning which choice yields the best convergence for a given dataset is lacking, even though statistical confidence bounds can be derived for computed SPOD gains (Schmidt & Colonius 2020). In general, estimation parameters are chosen subjectively based on the researcher's experience and convergence is checked *a posteriori*.

Moreover, mode convergence can be slow and difficult to verify as the method requires long time-resolved datasets. For Navier–Stokes simulations, this translates to high computational and storage costs that are often impracticable. A proposed alternative to reduce overall requirements of memory is the streaming SPOD algorithm proposed by Schmidt & Towne (2019). By accessing only one temporal snapshot at a time and incrementing the SPOD at each step, the algorithm allows for the use of arbitrarily long time series and real-time processing, avoiding storage costs, but maintaining long computations that may be expensive.

This work discusses the effects of estimation parameters on the convergence of the SPOD method. We first examine a model Ginzburg–Landau system which mimics the dynamics of turbulent jets. In sequence, the results from this convergence analysis are used to propose a new method based on a temporal shift to further reduce SPOD errors and enable a more accurate analysis of simulations with shorter integration times. In order to demonstrate its applicability to fluid flows, the shifting algorithm is applied to a boundary layer over a flat plate subject to bypass transition.

For flat-plate boundary layers, modal transition by Tollmien–Schlichting waves is bypassed for free-stream turbulence levels greater than around 1 % (Matsubara & Alfredsson 2001) as the transition occurs from the linear growth of streamwise elongated, low-frequency structures, with alternating high and low velocity, called streaks. The work of Ellingsen & Palm (1975) shows that perturbations in flows with low variation along the streamwise direction can be algebraically amplified through the transient growth caused by the interaction of non-normal Orr–Sommerfeld modes, even in cases where modal stability predicts an exponential decay. This phenomenon is known in the literature as the lift-up effect (Brandt 2014). In bypass conditions, the streaks caused by the lift-up effect might be amplified enough to trigger nonlinear interactions and degenerate to turbulence in Reynolds numbers below the critical levels provided by the linear theory of exponential growth (Brandt, Schlatter & Henningson 2004).

Streaks appear as SPOD modes with vanishing frequency (Sasaki *et al.* 2020), and numerical convergence in such cases is challenging (Pickering *et al.* 2020). Hence, detection of coherent structures in a database of bypass transition of a boundary layer is a relevant test of convergence of SPOD modes and of the potential improvements that may be obtained with the proposed temporal shift of the database.

The remainder of the manuscript is organised as follows. Sections 2 and 3 review methods used in SPOD and resolvent analysis. In § 4 the temporal shift is introduced and its effects are discussed, with guidance on how to choose shifting parameters. Finally, in § 5 the results of the application of these concepts in the Ginzburg–Landau system and the flat-plate case are evaluated.

2. Spectral POD

Spectral POD is a modal analysis method aimed at extracting the most energetic turbulent coherent structures which evolve in a single frequency from statistically stationary data. A brief explanation of the algorithm is developed in this section. The computation involves the snapshot method, and further information can be found in Towne *et al.* (2018) and Schmidt & Colonius (2020).

Considering a turbulent flow dataset with M degrees of freedom (number of variables times number of spatial points N_x) and N_t snapshots taken at a fixed interval δt (each one treated as an independent realisation based on the ergodicity argument), we define the state vector $\boldsymbol{q} \in \mathbb{C}^M$ with a chosen inner product as

$$\langle \boldsymbol{q}_1, \boldsymbol{q}_2 \rangle_{\boldsymbol{W}} = \boldsymbol{q}_1^H \boldsymbol{W} \boldsymbol{q}_2, \tag{2.1}$$

where $\boldsymbol{W}^{M\times M}$ is a square positive definite diagonal matrix, and $\{\cdot\}^H$ is the conjugate transpose. The ensemble of realisation vectors are then used to construct the data matrix

$$\boldsymbol{Q} = \begin{bmatrix} | & | & & | \\ \boldsymbol{q}_1 & \boldsymbol{q}_2 & \cdots & \boldsymbol{q}_{N_t} \\ | & | & & | \end{bmatrix}, \quad \boldsymbol{Q} \in \mathbb{C}^{M\times N_t}. \tag{2.2}$$

For the case of an incompressible flow, each component of the velocity field $\boldsymbol{u}(\boldsymbol{x}, t) = (u(\boldsymbol{x}, t), v(\boldsymbol{x}, t), w(\boldsymbol{x}, t))$ is a variable. In that case, we can construct the vector $\boldsymbol{q} \in \mathbb{C}^{3N_x}$ by computing the zero-mean velocity fluctuations for each snapshot, i.e.

$$\tilde{\boldsymbol{u}}(\boldsymbol{x}, t) = \boldsymbol{u}(\boldsymbol{x}, t) - \boldsymbol{U}(\boldsymbol{x}) = (\tilde{u}(\boldsymbol{x}, t), \tilde{v}(\boldsymbol{x}, t), \tilde{w}(\boldsymbol{x}, t)), \tag{2.3}$$

with $\boldsymbol{U}(\boldsymbol{x})$ being the mean field, and subsequently mapping all fluctuation components to a column vector in a convenient order, for example,

$$\boldsymbol{q}_i = \begin{bmatrix} \tilde{u}(\boldsymbol{x}_1, i) & \cdots & \tilde{u}(\boldsymbol{x}_{N_x}, i) & \tilde{v}(\boldsymbol{x}_1, i) & \cdots & \tilde{v}(\boldsymbol{x}_{N_x}, i) & \tilde{w}(\boldsymbol{x}_1, i) & \cdots & \tilde{w}(\boldsymbol{x}_{N_x}, i) \end{bmatrix}^{\mathrm{T}}. \tag{2.4}$$

2.1. *Spectral estimation*

For the estimation of the CSD matrix $\boldsymbol{C}$, the Welch method is employed. The data matrix $\boldsymbol{Q}$ is decomposed into N_b successive blocks containing N_{FFT} realisations, with O_{FFT} overlapped realisations between consecutive blocks. Then, the discrete Fourier transform (DFT) in time, weighted by a windowing function $w(t)$, is computed for each block.

Given $\hat{\boldsymbol{q}}_k(\omega)$, the vector resulting from the DFT at a frequency ω for the kth block, we can assemble the vectors from all blocks corresponding to this frequency in a spectral data matrix

$$\hat{\boldsymbol{Q}}_\omega = \begin{bmatrix} | & | & & | \\ \hat{\boldsymbol{q}}_1 & \hat{\boldsymbol{q}}_2 & \cdots & \hat{\boldsymbol{q}}_{N_b} \\ | & | & & | \end{bmatrix}, \quad \hat{\boldsymbol{Q}}_\omega \in \mathbb{C}^{M\times N_b}, \tag{2.5}$$

allowing the CSD matrix for each frequency to be computed as

$$\boldsymbol{C}_\omega = \frac{1}{N_b} \hat{\boldsymbol{Q}}_\omega \hat{\boldsymbol{Q}}_\omega^H \boldsymbol{W}, \quad \boldsymbol{C}_\omega \in \mathbb{C}^{M\times M} \tag{2.6}$$

and finally SPOD gains $\hat{\boldsymbol{\Lambda}}$ and modes $\hat{\boldsymbol{\Psi}}$ are calculated by solving the following eigenproblem of size $M \times M$:

$$\boldsymbol{C}_\omega \hat{\boldsymbol{\Psi}} = \hat{\boldsymbol{\Psi}} \hat{\boldsymbol{\Lambda}}. \tag{2.7}$$

2.2. *Snapshot SPOD*

In fluid dynamics applications datasets often have $M \gg N_b$, as the problems are typically high dimensional and the cost of their simulation typically limits the amount of snapshots that can be obtained and handled. Therefore, it is computationally cheaper to obtain the same modes and gains by solving the much smaller eigenproblem of size $N_b \times N_b$ in the row space of the matrix $\hat{\boldsymbol{Q}}_\omega$, as presented by Sirovich (1987) and revisited in Towne *et al.* (2018),

$$\boldsymbol{M}_\omega = \frac{1}{N_b}\hat{\boldsymbol{Q}}_\omega^H \boldsymbol{W}\hat{\boldsymbol{Q}}_\omega, \quad \boldsymbol{M}_\omega \in \mathbb{C}^{N_b \times N_b}, \tag{2.8}$$

$$\boldsymbol{M}_\omega \hat{\boldsymbol{\Theta}} = \hat{\boldsymbol{\Theta}}\hat{\boldsymbol{\Lambda}}, \tag{2.9}$$

$$\hat{\boldsymbol{\Psi}} = \frac{1}{\sqrt{N_b}}\hat{\boldsymbol{Q}}_\omega \hat{\boldsymbol{\Theta}}\hat{\boldsymbol{\Lambda}}^{-1/2}. \tag{2.10}$$

3. Resolvent analysis

When applying the Reynolds decomposition to the Navier–Stokes equation, linear and nonlinear terms can be isolated. Then, nonlinear terms may be treated as an input forcing signal to a linear system. In other words, we construct a state-space formulation with input/forcing terms $\boldsymbol{f}$ related to response/fluctuations terms $\boldsymbol{q}$ by a linear operator $\boldsymbol{L}$ that is only a function of time invariant parameters, considering a linearisation of the Navier–Stokes system around a laminar solution (Jovanović & Bamieh 2005) or a mean flow (McKeon & Sharma 2010). Operators $\boldsymbol{H}$ and $\boldsymbol{B}$ are used to restrict spatially the forcing and response, respectively, when necessary. We thus have

$$\left.\begin{aligned} \frac{\partial \boldsymbol{q}}{\partial t} &= \boldsymbol{L}\boldsymbol{q} + \boldsymbol{B}\boldsymbol{f}, \\ \boldsymbol{y} &= \boldsymbol{H}\boldsymbol{q}, \end{aligned}\right\} \tag{3.1}$$

and by taking the Fourier transform in time we obtain

$$\left.\begin{aligned} (\mathrm{i}\omega \boldsymbol{I} - \boldsymbol{L})\,\hat{\boldsymbol{q}} &= \boldsymbol{B}\hat{\boldsymbol{f}}, \\ \hat{\boldsymbol{y}} &= \boldsymbol{H}\hat{\boldsymbol{q}}, \end{aligned}\right\} \tag{3.2}$$

$$\hat{\boldsymbol{y}} = \boldsymbol{R}\hat{\boldsymbol{f}} \implies \boldsymbol{R} = \boldsymbol{H}\,(\mathrm{i}\omega \boldsymbol{I} - \boldsymbol{L})^{-1}\,\boldsymbol{B}, \tag{3.3}$$

where $\boldsymbol{R}$ is called the resolvent operator. Now, resolvent response modes $\boldsymbol{U}$, forcing modes $\boldsymbol{V}$ and gains $\boldsymbol{\Sigma}$ (ratio between the norms of $\boldsymbol{y}$ and $\boldsymbol{f}$) can be computed via the singular value decomposition (SVD)

$$\tilde{\boldsymbol{R}}\tilde{\boldsymbol{V}} = \tilde{\boldsymbol{U}}\boldsymbol{\Sigma}. \tag{3.4}$$

From the resolvent framework (3.3), the response CSD matrix $\boldsymbol{C}_\omega$ can be computed directly as a function of the forcing CSD matrix $\boldsymbol{F}_\omega$. Assuming that

$$\boldsymbol{C}_\omega = \mathcal{E}\left(\hat{\boldsymbol{y}}\hat{\boldsymbol{y}}^H\right), \quad \boldsymbol{F}_\omega = \mathcal{E}\left(\hat{\boldsymbol{f}}\hat{\boldsymbol{f}}^H\right), \tag{3.5a,b}$$

where $\mathcal{E}(\cdot)$ stands for the average over all realisations, we have

$$\boldsymbol{C}_\omega = \boldsymbol{R}\boldsymbol{F}_\omega\boldsymbol{R}^H. \tag{3.6}$$

If forcing terms are perfectly uncorrelated, $\boldsymbol{F}_\omega = \boldsymbol{I}$, the expression can be reduced to

$$\boldsymbol{C}_\omega = \boldsymbol{R}\boldsymbol{R}^H \tag{3.7}$$

and, from (3.4), we have

$$\boldsymbol{C}_\omega = \boldsymbol{U}\boldsymbol{\Sigma}^2\boldsymbol{U}^{-1} \implies \boldsymbol{C}_\omega\boldsymbol{U} = \boldsymbol{U}\boldsymbol{\Sigma}^2 \tag{3.8}$$

leading to

$$\hat{\boldsymbol{\Psi}} = \boldsymbol{U}, \quad \hat{\boldsymbol{\Lambda}} = \boldsymbol{\Sigma}^2 \tag{3.9a,b}$$

from (2.7).

This shows that resolvent response modes are equal to those obtained via the SPOD method for a system forced with spatially white forcing (Towne *et al.* 2018), a property also true for an arbitrary inner-product norm (see Appendix A).

In this study the mode equivalence property is exploited to study numerically the convergence of SPOD modes by employing a simple linear system analogous to the Navier–Stokes system, forced with spatially uncorrelated signals, and comparing resolvent and SPOD results.

4. Temporal shift

The idea of introducing a temporal shift to compensate for transport in signal processing and modal decomposition is not new. The work of Reiss *et al.* (2018), for instance, discusses its application on the construction of ROMs and proposes a shifted method based on spatial POD to address the slow decay of energy observed from the modal decomposition of transport dominated phenomena. However, to the best of our knowledge, the application of a time delay in SPOD has not been attempted.

The Welch method employed in the SPOD method separates the dataset in blocks of a chosen time length. For transport dominated phenomena with elongated domains, one can usually choose signals corresponding to coordinates $\boldsymbol{x_1}$ and $\boldsymbol{x_2}$ where the time lag for peak cross-correlation is greater than the block time length. The effect is shown in figure 1 with the blue rectangle, which illustrates the standard situation where the same initial and final times of Welch blocks are taken for all positions in the flow. This causes an apparent loss of coherence and encumbers the statistical convergence of the decomposition. This feature was observed, for instance, by Jaunet, Jordan & Cavalieri (2017).

4.1. *Proposed algorithm*

In order to address the limitations imposed by the Welch method, we propose an extension to the SPOD algorithm in two steps, exploiting the assumed stationarity: we first apply a shift in time and then correct the phase in Fourier space, in a procedure that preserves asymptotic convergence to the true CSD (see Appendix B). The temporal shift aims at improving convergence for a window of finite size by maximising cross-correlations within each Welch block, via the insertion of an expected time delay to each spatial location.

Concerning the SPOD implementation, first we treat the data matrix $\boldsymbol{Q}$ by means of a data shift and then correct the effects of this treatment after the application of the

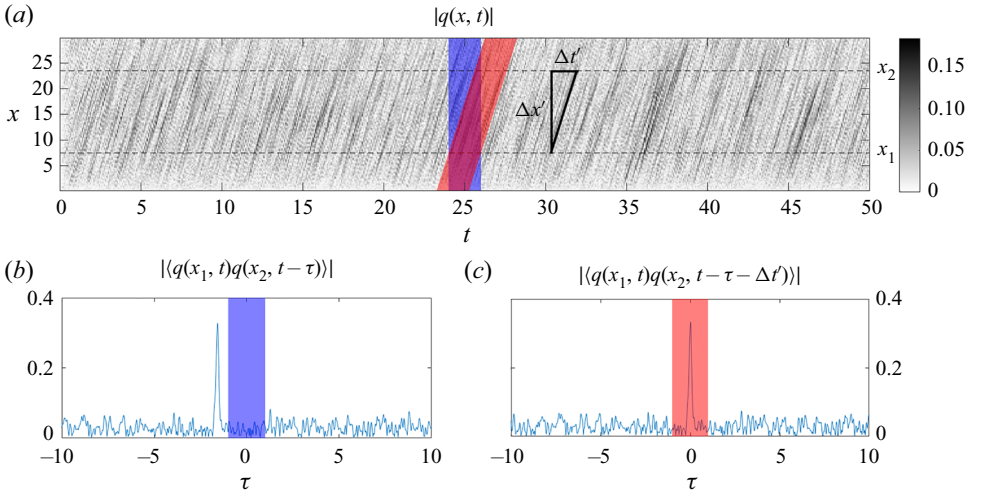

Figure 1. Diagram illustrating the effect of the temporal shift on the model system presented in § 5.1. In standard conditions, the cross-correlation peak lies outside the chosen time window. The application of the expected time lag between signals in positions x_1 and x_2 maintains the peak inside the same time window. The operator $\langle \cdot \rangle$ denotes the expected value.

Welch method. Given a point of interest with streamwise coordinate x_p and a matrix $\boldsymbol{Q}$ with N_x rows and N_t columns, for each row k, the columns are shifted by

$$s_k = \frac{\Delta x}{U_k \delta t}, \quad \Delta x = x_p - x_k \tag{4.1}$$

positions. In this expression x_k is the point's streamwise coordinate, δt is the time step between realisations and U_k is a chosen velocity so that $\Delta x/U_k$ approximates the time lag for peak cross-correlation with respect to the point of interest. For instance, the dominant convection velocity could be used, if this information is readily available. Moreover, there is no requirement for U_k to be constant throughout the domain.

Columns at the beginning or the end of the time series, for which the time shift s_k is not possible, are removed from the computation. This can be more easily implemented as a circular shift of the data removing the columns for which there is an artificial overlap between the end of the time series at one point and the beginning of the series at another point.

It is important to note that, if s_k is not an integer, the shift must be interpolated, as discussed in Reiss *et al.* (2018). Given $\mathcal{Z}_k^s$, the operator that circularly shifts a line k by s positions, and $\tilde{\boldsymbol{Q}}$ the resulting shifted matrix, the linearly interpolated shifting operation takes the form

$$\tilde{\boldsymbol{Q}} = \begin{cases} \mathcal{Z}_k^{s_k} \boldsymbol{Q} & \text{if } s_k \in \mathbb{Z}, \\ (\lceil s_k \rceil - s_k) \cdot \mathcal{Z}_k^{\lfloor s_k \rfloor} \boldsymbol{Q} + (s_k - \lfloor s_k \rfloor) \cdot \mathcal{Z}_k^{\lceil s_k \rceil} \boldsymbol{Q} & \text{otherwise.} \end{cases} \tag{4.2}$$

After application of the Welch method the kth row of each resulting $\hat{\boldsymbol{Q}}_\omega$ matrix, with N_x rows and N_b columns, is multiplied by $\exp(-\mathrm{i}\omega s_k \delta t)$ to correct the phase created by the previous temporal shift operation, according to the properties of the Fourier transform.

This procedure will be referred to in this work as a shifted SPOD, for the sake of concision, and should not be considered a new variety of POD, but instead a new algorithm for the method we call SPOD.

Computationally, the shifting algorithm deals with row-wise rearrangements of matrix elements and also row-wise array multiplications, which are low complexity operations when compared with Fourier transforms and eigenproblems. Once the data matrices are loaded in memory, both these steps should be rapidly performed on a modern desktop computer without the addition of expressive cost to the SPOD method.

4.2. *On the choice of point of interest, shifting velocity and window size*

The choice of window size N_{FFT} and, consequently, the number of blocks N_b is the most subjective step of the SPOD method. For a given database, it is not obvious how one should choose the most appropriate number of realisations per block that simultaneously ensures blocks are long enough in time to properly capture the evolution of the most energetic structures and numerous enough to reduce the decomposition's variance.

Here, we discuss this choice and propose a pre-processing analysis to objectively set a suitable N_{FFT} for a given dataset, considering a shifting velocity and point of interest. This procedure is also applicable to the standard SPOD, as it can be treated as a special case of the shifted SPOD with shifting velocity $U_k \to \infty$. The procedure follows four steps.

(i) Given a preferential flow direction X, we choose a point of interest p of coordinate x_p contained in the region from which we want to extract the most energetic structures. For simulations, it is important to avoid points under the influence of numerical boundaries, such as inlets, outlets and sponge/fringe zones, in order to guarantee that computed two-point correlations are physical.

(ii) Once p is chosen, we compute the space–time correlations at positions along the X direction with respect to the signal at x_p, as later illustrated in figure 4(a). In the case of multi-dimensional data, cross-correlations can be computed at multiple slices, as will be later shown in figure 14(a,c,e), or for multiple vector components.

(iii) The inclination of the peak correlations quantifies the dominant convection velocity, which might vary as a function of position and not necessarily match the local mean velocity (He, Jin & Yang 2017). By applying a shifting velocity that approximates said dominant velocity, it is possible to align correlation peaks, as later discussed in figures 4(b) and 14(b,d,f), in order to generate a vertical band of high correlation in time. This narrower correlation allows a given window to capture more kinematic information about the system. However, if a dominant velocity cannot be identified, the shifting operation should yield no special benefit.

(iv) From the space–time plot we are finally able to determine the smallest window size capable of capturing the bulk of correlation, which simultaneously resolves the frequencies of interest in the study. By narrowing the correlation band in time, the shifting algorithm admits even smaller window sizes for the same amount of correlation captured and, thus, reduces overall variance by increasing the number of blocks N_b. In this way, it becomes feasible to objectively set the N_{FFT} parameter based on the individual characteristics of each database and frequency resolution requirements.

5. Convergence analysis of SPOD

5.1. *A model problem: Ginzburg–Landau equation*

The complex-valued Ginzburg–Landau equation (CGLE) has been one of the most studied equations in a wide variety of physics fields to provide insight over the dynamics of non-equilibrium phenomena in spatially extended systems (Aranson & Kramer 2002).

Particularly in the field of fluid dynamics and turbulence, the one-dimensional linearised complex Ginzburg–Landau equation is often employed to model instabilities in spatially evolving flows for its properties of advection and diffusion (Huerre & Monkewitz 1990; Bagheri *et al.* 2009; Cavalieri, Jordan & Lesshafft 2019). The equation is written in the input–output framework as

$$\frac{\partial \boldsymbol{q}}{\partial t} + U\frac{\partial \boldsymbol{q}}{\partial x} - \mu(x)\boldsymbol{q} - \gamma\frac{\partial^2 \boldsymbol{q}}{\partial x^2} = \boldsymbol{f}, \tag{5.1}$$

with $\boldsymbol{q}$ and $\boldsymbol{f}$ being output response and input forcing, respectively, and rewritten in Fourier space as

$$\left(\mathrm{i}\omega\boldsymbol{I} + U\frac{\partial}{\partial x} - \mu(x) - \gamma\frac{\partial^2}{\partial x^2}\right)\hat{\boldsymbol{q}} = \hat{\boldsymbol{f}} \tag{5.2}$$

from which the resolvent operator can be computed as

$$\boldsymbol{R} = \left(\mathrm{i}\omega\boldsymbol{I} + U\frac{\partial}{\partial x} - \mu(x) - \gamma\frac{\partial^2}{\partial x^2}\right)^{-1} \tag{5.3}$$

with an inverse obtained after a discretisation of the derivatives to form the operators in matrix form.

When the system is forced with spatially white statistics on a given frequency ω, the SPOD modes $\hat{\boldsymbol{\psi}}(\omega)$ are identical to the resolvent response modes, $\boldsymbol{u}(\omega)$. Thus, such response modes, which are deterministic in nature, are used to quantify the SPOD convergence defined in terms of the error

$$\varepsilon(\omega) = 1 - \frac{|\langle\hat{\boldsymbol{\psi}}(\omega), \boldsymbol{u}(\omega)\rangle|}{\|\hat{\boldsymbol{\psi}}(\omega)\| \cdot \|\boldsymbol{u}(\omega)\|}, \tag{5.4}$$

where the operators $\langle\cdot,\cdot\rangle$ and $\|\cdot\|$ are respectively the Euclidean inner product and norm.

The model problem was devised according to Cavalieri *et al.* (2019) and parameters

$$\mu(x) = A\left(1 - \frac{x}{10}\right), \tag{5.5}$$

$$\gamma = \frac{1-\mathrm{i}}{10}, \tag{5.6}$$

were set to mimic the dynamics of turbulent jets. Three distinct cases were investigated: case 1 with $U = 10$ and $A = 0.6$; case 2 with $U = 12$ and $A = 1$; case 3 with $U = 14$ and $A = 1.25$. These choices lead to a varying convection velocity between the three cases, which modifies the correlation peaks discussed in § 4. Numerical solutions were obtained using a Crank–Nicolson scheme for time marching. Spatial discretisation was set using a fixed grid spacing of $\Delta x = 0.1$, with a total of $N_x = 300$ points, $x \in [0, 30]$ and $q(0) = q(30) = 0$. A second-order upwind scheme was applied for the first spatial derivative and a second-order centred scheme for the second. Because of the uniform grid, the inner-product matrix $\boldsymbol{W}$ is set as $I\Delta x$ to account for the spatial quadrature.

The forcing is applied by adding a random complex number with a uniformly distributed phase and amplitude to the value at each grid point for every time step. To ensure that fluctuations are adequately resolved in frequency, we apply to the forcing signal a finite impulse response low-pass filter of 30th order in time, with cutoff at 60 % of the Nyquist frequency. Numerical integration is done for a range of 500 time units using a time step of $\delta t = 0.01$, generating a total of $N_t = 5 \times 10^4$ snapshots per case.

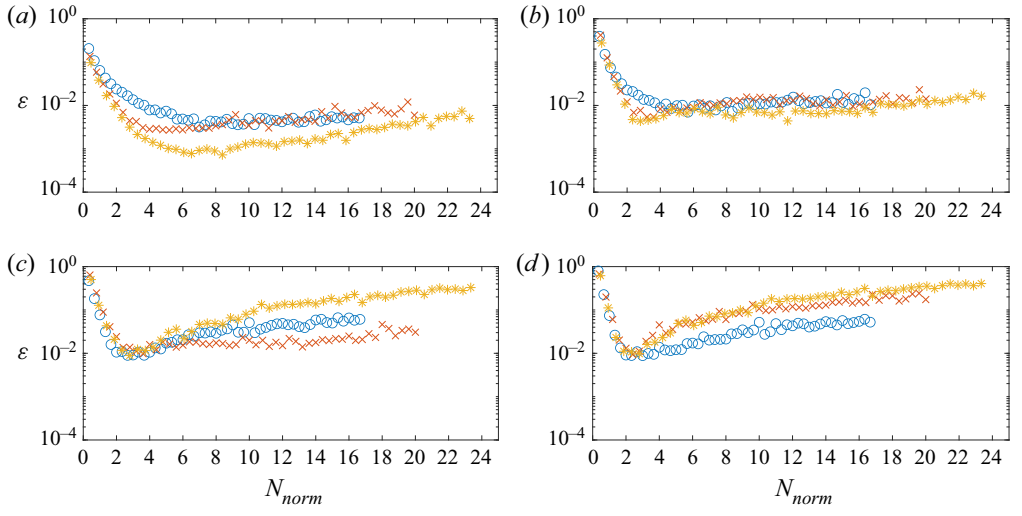

Figure 2. Spectral POD estimation error ε at frequency $\omega = 2\pi$, plotted against the normalised window length N_{norm}. Legend: (○, blue) case 1; (×, red) case 2; (∗, orange) case 3. (*a*) Mode 1; (*b*) mode 2; (*c*) mode 3; (*d*) mode 4.

5.1.1. *Computation of SPOD modes*

In order to understand how SPOD errors scale as a function of sampling and estimation parameters for each model case, the number of snapshots N_{FFT} within each block is varied from 100 to 5000 in steps of 100 and the number of blocks N_b set accordingly to comprise all N_t snapshots (fixed-data analysis). This configuration ensures that all computations reach exactly the frequency $\omega = 2\pi$, which has the same order of magnitude of the most energetic frequency in all three cases, in order to compare SPOD and resolvent modes.

To reduce spectral leakage effects and allow for the use of a relatively large consecutive block overlapping of $O_{FFT} = \lfloor 0.75\, N_{FFT} \rfloor$, we apply to each block an infinitely smooth windowing function of the form

$$w_{C_2^\infty}(t) = \begin{cases} e^8 / e^{2T^2/(t(T-t))}, & 0 < t < T, \\ 0 & \text{otherwise}, \end{cases} \tag{5.7}$$

with all derivatives equal to zero at 0 and T (Martini *et al.* 2020).

The error between SPOD and resolvent modes, defined in (5.4), is shown in figure 2 for the leading four SPOD modes at frequency $\omega = 2\pi$. The results obtained indicate that better absolute convergence is related to window length, normalised by domain size, and convection velocity. Thus, we define a normalised window size

$$N_{norm} = \frac{N_{FFT}\delta t}{T_c}, \quad T_c = \frac{L}{U}, \tag{5.8}$$

where T_c is the time taken to cross the entire domain based on the parameter U of the CGLE system and L is the total length of the domain.

The graphs in figure 2 show that SPOD modes computed with very low values of N_{norm} yield the worst convergence. In that scenario, the Welch blocks are too short to correctly capture the evolution of coherent structures in time, which leads to statistically biased results. On the other side, for larger N_{norm} values, errors tend to stabilise or even increase

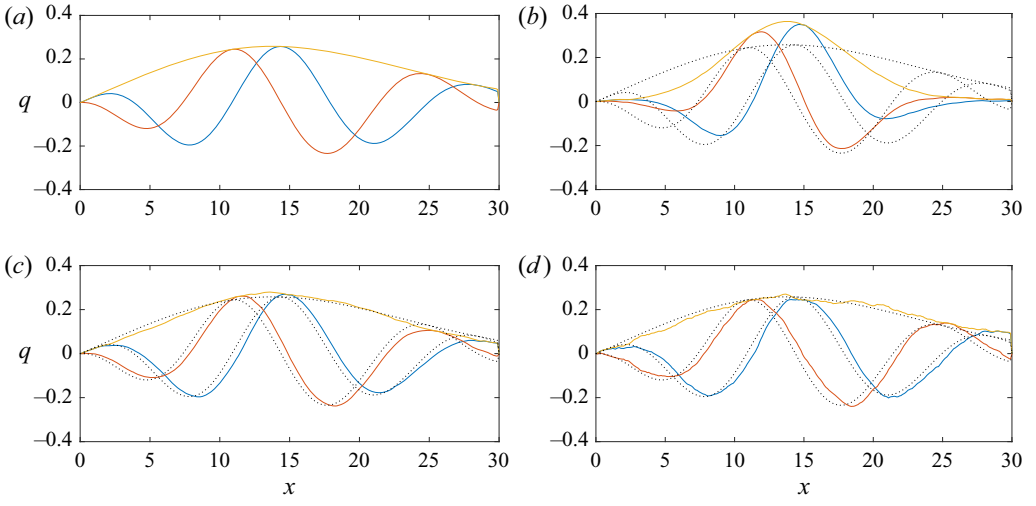

Figure 3. Mode 1 at frequency $\omega = 2\pi$ for case 3. Other cases display similar features. (*a*) Resolvent operator response mode; (*b*) SPOD mode with $N_{FFT} = 100$, $N_b = 1997$ and $N_{norm} \approx 0.5$: higher precision, lower accuracy (bias); (*b*) SPOD mode with $N_{FFT} = 600$, $N_b = 330$ and $N_{norm} \approx 3$; (*c*) SPOD mode with $N_{FFT} = 5000$, $N_b = 37$ and $N_{norm} \approx 23$: lower precision, higher accuracy (noise). Legend: (orange) absolute value; (blue) real part; (red) imaginary part; (dotted lines) resolvent mode for comparison.

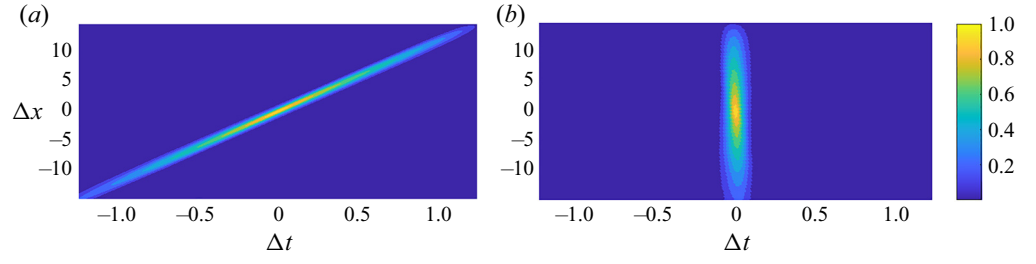

Figure 4. Space–time cross-correlation with respect to the point $x_p = 15$ for case 2 ($U = 12$, $A = 1$). Other cases display similar features. (*a*) No shift; (*b*) optimal shift.

for higher modes (modes 3 and 4) due to the reduced number of averaging blocks and consequent increase in noise.

A trade-off between estimation bias, which is reduced with increasing window sizes, and estimation variance, i.e. statistical noise, which increases with window size (lower number of samples), is thus required. Effects of bias and noise are illustrated in figure 3.

Overall, a normalised window size between 2 and 4 is a good compromise to achieve the best convergence across the first four SPOD modes in these cases. This implies that a time series should be sufficiently long to comprise a large number of blocks of normalised window size between 2 and 4. This would translate to a database with several flow-through times, which may be quite expensive to compute and store if one deals with complex flows. In what follows we will explore how the temporal shift of § 4 may alleviate such requirements.

5.1.2. *Application of the temporal shift*

The analysis of § 5.1.1 was also performed using the shifted SPOD algorithm. Parameters N_{FFT}, N_b and O_{FFT} were set in the same exact manner, as well as the windowing function.

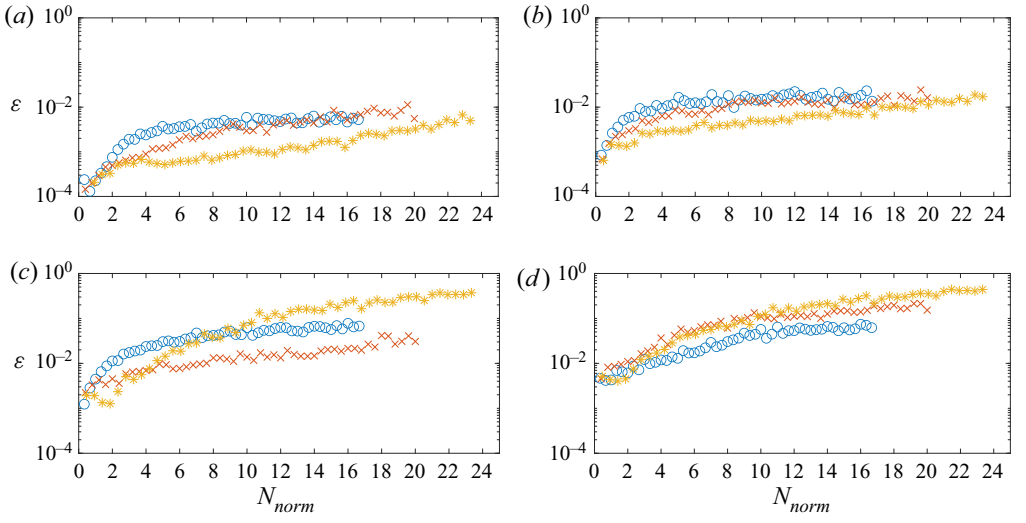

Figure 5. Shifted SPOD estimation error ε at frequency $\omega = 2\pi$, plotted as a function as N_{norm}. Legend: ($\circ$, blue) case 1; ($\times$, red) case 2; ($*$, orange) case 3. (*a*) Mode 1; (*b*) mode 2; (*c*) mode 3; (*d*) mode 4.

Each case was shifted with respect to the point of interest $x_p = 15$, in the middle of the numerical domain, according to the algorithm of § 4. The parameter U of the corresponding CGLE was applied as the optimal shifting velocity for all points, in a operation that approximates almost exactly the peak cross-correlation, as it is shown in figure 4. In this graph a Welch block window can be represented as a vertical band, consisting of all Δx and a limited Δt. From this observation it is possible to conclude that a narrow window can contain more correlation in the shifted case.

The results obtained are shown in figure 5. Compared with figure 2, estimation errors ε are greatly reduced for the lowest values of N_{norm}, which means that the shifting operation is successful in reducing the bias observed with shorter Welch blocks, an effect illustrated in figure 6. Thus, the approach considerably alleviates the trade-off between bias and variance discussed in the previous section.

One should note that, in these cases, where the correlation between signals falls sharply for time lags which do not match the convection velocity (figure 4), the minimal time window able to resolve the studied frequency is successful in reducing the bias. However, it is expected that, in more general cases, containing a wide range of coherent structures and nonlinear dynamics, the narrowest time windows able to resolve a given frequency should still lead to errors, as they might not contain a relevant part of the correlation function.

5.1.3. *Comparison with fixed variance*

We compare standard and shifted SPOD algorithms when a fixed number of blocks N_b is considered and only the window size N_{FFT} is changed. Contrary to the previous analysis, this set-up does not consider all of the snapshots available in the dataset, as the SPOD algorithm will require fewer snapshots for smaller window sizes and the same quantity of blocks. The variance of the estimates is kept approximately constant, allowing for a study of the effect of estimation bias. We choose $N_b = 100$ and sweep N_{FFT} values from 100 to 1900 in steps of 100. The overlap value O_{FFT} and windowing function $w(t)$ remain unchanged.

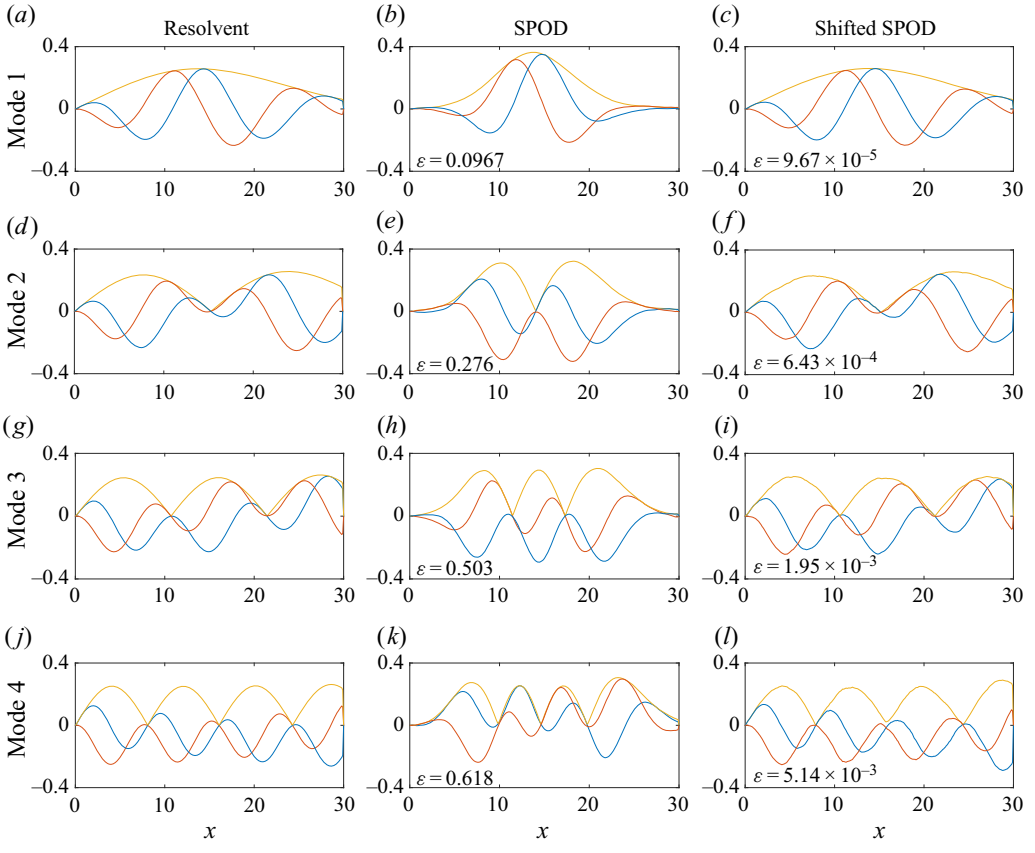

Figure 6. Comparison between resolvent, SPOD and shifted SPOD modes, at frequency $\omega = 2\pi$, for case 3. All SPOD modes were computed with $N_{FFT} = 100$ and $N_{norm} \approx 0.5$. Other cases display similar features. Legend: (orange) absolute value; (blue) real part; (red) imaginary part.

Figure 7 shows the results of this fixed-block analysis. Estimation errors for the shifted SPOD are always smaller than those of the standard SPOD, with effects more pronounced in the region of smaller window size N_{FFT}, where a reduction of at least one order of magnitude is observed in some cases.

An expressive reduction in estimation error for smaller N_{FFT} values induced by the shifted SPOD algorithm is relevant because, for a given number of Welch blocks, it allows for a more precise and accurate computation of the most energetic modes on datasets with short time lengths, as is typical for large simulations, and reduces the sensitivity of the method to the window size parameter.

5.1.4. *Comparison with fixed window size*

We also compare standard and shifted SPOD algorithms considering a fixed window size N_{FFT}, where only the number of blocks N_b is changed. As in the previous analysis, this set-up does not consider all of the snapshots available in the dataset. We choose $N_{FFT} = 100$, which corresponds to $N_{norm} < 1$ for all three cases, and sweep N_b values from 20 to 800 in steps of 20. Again, the overlap value O_{FFT} and windowing function $w(t)$ remain unchanged.

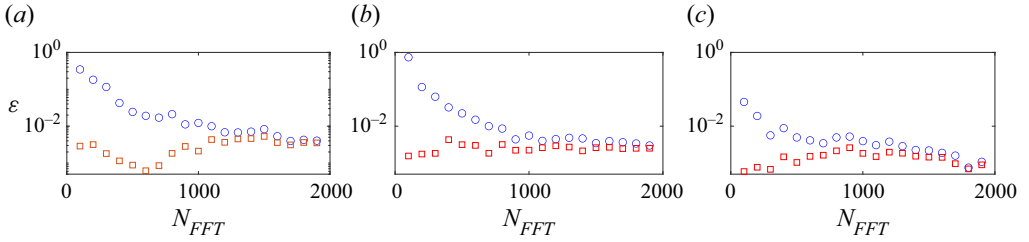

Figure 7. Estimation error ε of mode 1, at frequency $\omega = 2\pi$ and number of blocks $N_b = 100$, as a function of the window size N_{FFT}. Legend: (○, blue) standard SPOD; (□, red) shifted SPOD. (*a*) Case 1; (*b*) case 2; (*c*) case 3.

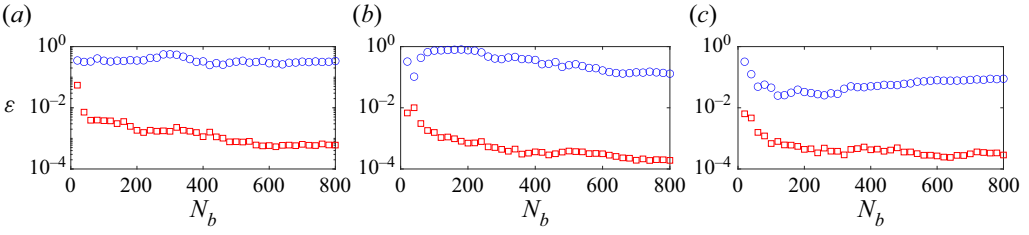

Figure 8. Estimation error ε of mode 1, at frequency $\omega = 2\pi$ and number of snapshots $N_{FFT} = 100$, as a function of the number of blocks N_b. Legend: (○, blue) standard SPOD; (□, red) shifted SPOD. (*a*) Case 1; (*b*) case 2; (*c*) case 3.

Figure 8 shows the results of the fixed window analysis. For the case of a small window size, not long enough in time to properly capture the system dynamics, the standard SPOD algorithm is not capable of reducing estimation errors with the increase of the time series length (and, consequently, the number of blocks) to the level of the shifted algorithm, which shows significantly lower errors.

5.1.5. *Effect of non-optimal shifting velocities*

All previous analysis focused on the optimal shift, equal to the known single convection velocity in each case. However, in most fluid dynamics applications different scales propagate at different velocities. Moreover, as stated in § 4.2, the convection of coherent structures might vary as a function of position and not necessarily match the local mean velocity, making the exact correspondence between shifting and convection velocities impractical.

To study the effects of a non-optimal shift, we compare the errors ε of shifted SPOD modes computed with different shifting velocities U_{shift}. Figure 9 shows the results of this analysis, where it is clear that the lowest error is achieved when shifting and convection velocities are equal.

According to (4.1), the shift is inversely proportional to shifting velocity. For smaller than optimal U_{shift}, the algorithm overestimates the necessary shift and errors rise sharply, as $U_{shift} \to 0$ and $s_k \to \infty$, reaching levels higher than the standard SPOD. Due to this behaviour, very low shifting velocities should be applied with special care, even though the use of very low convection velocities is rare, as quantities are often normalised.

Inversely, $U_{shift} \to \infty$ leads to $s_k \to 0$, implying shifted and standard SPODs are asymptotically identical, with errors following this same trend. In other words, assuming

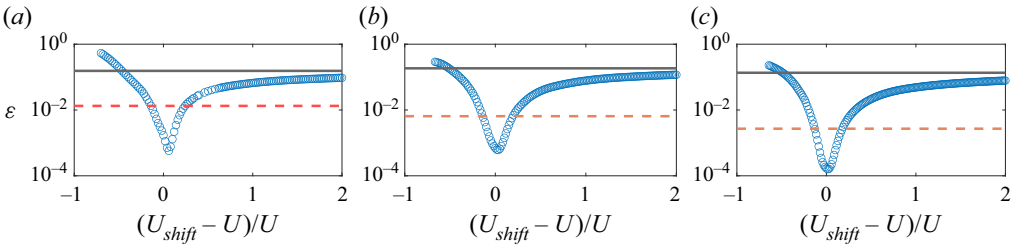

Figure 9. Estimation error ε of mode 1, at frequency $\omega = 2\pi$, number of snapshots $N_{FFT} = 100$ and entire time series, as a function of the shifting velocity U_{shift}. Legend: (−) standard SPOD; (−−, red) random $U_{shift}(x) \in [0.8\,U, 1.2\,U]$ shifted SPOD; (○, blue) constant U_{shift} shifted SPOD. (*a*) Case 1; (*b*) case 2; (*c*) case 3.

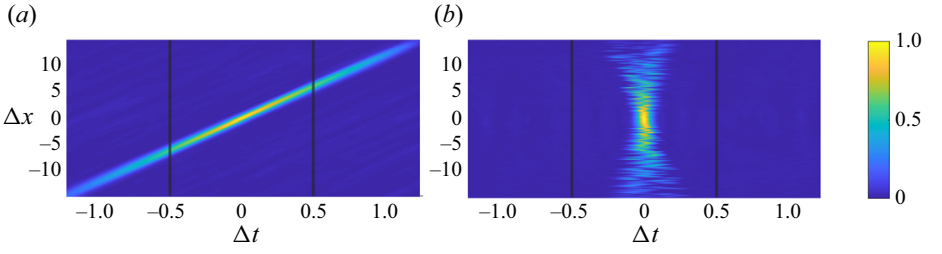

Figure 10. Space–time cross-correlation with respect to the point $x_p = 15$ for case 2 ($U = 12, A = 1$). Vertical lines represent the bounds of a window of size $N_{FFT} = 100$. Other cases display similar features. (*a*) No shift; (*b*) random $U_{shift}(x) \in [0.8\,U, 1.2\,U]$.

errors grow monotonically with the increase of $U_{shift} - U$, the shifted SPOD will always return better converged results than the standard algorithm for larger than optimal U_{shift}. This property can be exploited in the case of a flow with multiple known convection scales propagating to the same direction: by setting the shifting velocity to the largest convection velocity, error reduction should be obtained for all scales, albeit at different levels.

Finally, we consider a random shift where $U_{shift}(x) \in [0.8\,U, 1.2\,U]$, whose space–time correlation map is displayed in figure 10. Even though the shift is not constant nor optimal, it still efficiently reduces errors by maintaining the bulk of correlation within the window size bounds. With this set-up we stress that the shifting velocity is not physical and not limited by conditions of continuity and smoothness, as phases in the Fourier space are corrected point by point, individually. Furthermore, we show that the exact match between shifting and local convection velocities is not a requirement, but rather a condition for optimal error reduction.

5.1.6. *Effect on different frequencies*

In a last analysis, we divert the focus from the frequency $\omega = 2\pi$ used in previous results to discuss the effect of the shifted SPOD on the ensemble of frequencies.

Figure 11 illustrates SPOD power spectra computed from the sum of eigenvalues at each frequency for case 3. As we consider the CGLE, the full spectrum of positive and negative frequencies is considered. At $N_{norm} = 1$, the errors of modes at frequency $\omega = 2\pi$ for shifted and non-shifted methods are at least an order of magnitude apart. However, for both $N_{norm} = 1$ and $N_{norm} = 15$, the methods yield almost identical spectra, with discrepancies arising only for higher, less energetic frequencies.

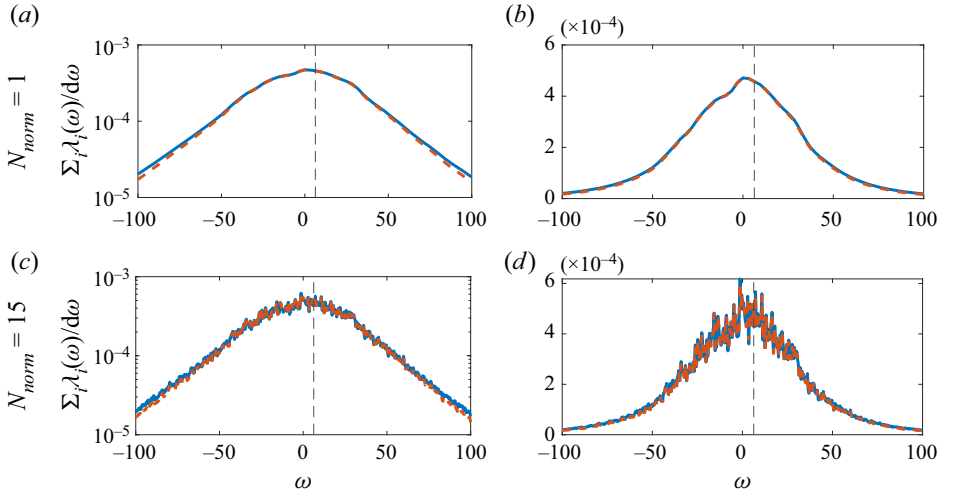

Figure 11. Spectral POD power spectra for case 3. Other cases display similar features. Legend: (blue) standard SPOD, (red) shifted SPOD, (−−) $\omega = 2\pi$.

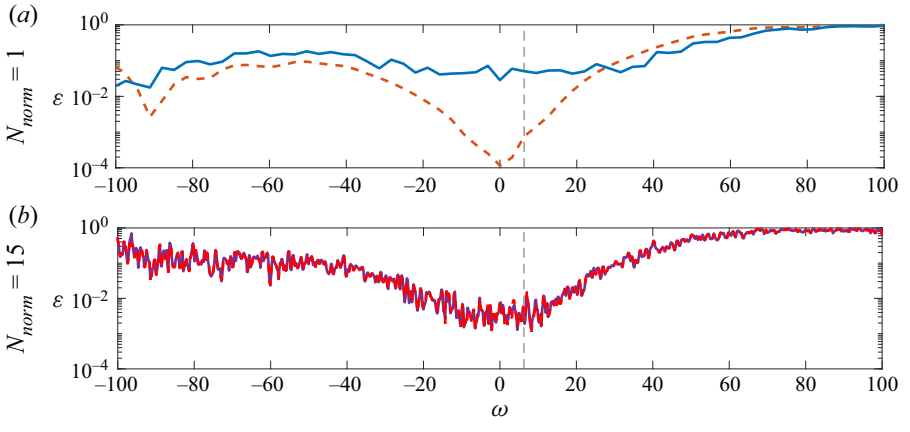

Figure 12. Estimation errors ε as a function of frequency for case 3. Other cases display similar features. Legend: (blue) standard SPOD, (red) shifted SPOD, (−−) $\omega = 2\pi$.

The behaviour of mode convergence can be further analysed in figure 12, where estimation errors ε are plotted with respect to the frequency. For a larger window size ($N_{norm} = 15$), both shifted and standard algorithms converge to the same behaviour in frequency, corroborating the properties deduced in Appendix B. On the other hand, at $N_{norm} = 1$, the most significant impact of the shifted SPOD is perceived close to the lowest frequencies, a region where the energy separation is the greatest and where the standard SPOD achieves better convergence at $N_{norm} = 15$. In a typical Navier–Stokes solution these low frequencies correspond to the largest and most energetic scales.

5.2. *Transitional boundary layer over a flat plate*

In this section the SPOD and resolvent methods are applied to study the most energetic/amplified structures present in a stable boundary layer subject to transient growth

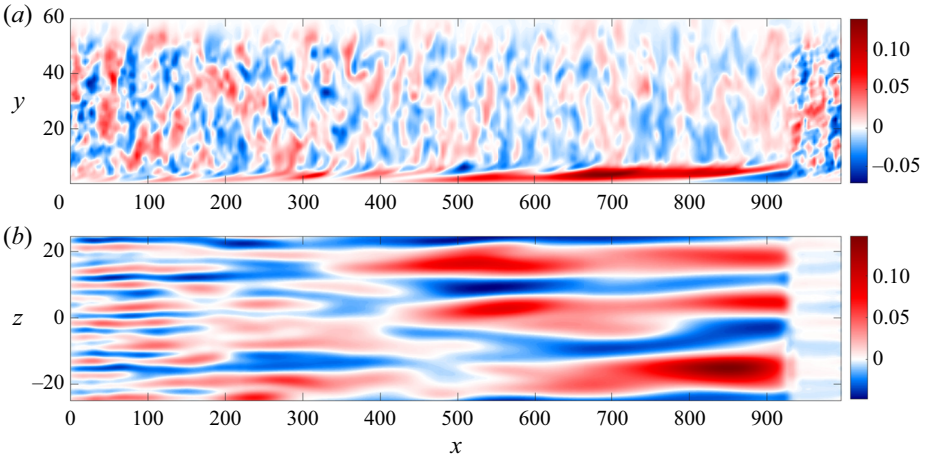

Figure 13. Snapshot of the LES, where elongated structures can be observed inside the boundary layer. Colours represent the streamwise velocity component. (*a*) Slice at $z = 0$. (*b*) Slice at $y = 0.8$. The fringe zone is visible after $x = 900$.

prior to bypass transition. The case will serve as a numerical application of the concepts discussed in previous sections.

The database used for this analysis was generated using the SIMSON solver (Chevalier, Lundbladh & Henningson 2007). A large-eddy simulation (LES) of the transitional region of a Blasius-type boundary layer is carried out for the flow over a flat plate without leading edge and subject to no pressure gradient. This same database has already been validated and produced results in previous works (Sasaki *et al.* 2020).

The computational domain (figure 13) consists of a $231 \times 121 \times 108$ ($X \times Y \times Z$) grid, composed by Chebyshev nodes in the direction perpendicular to the wall and homogeneously spaced points in the other two directions, which are discretised with Fourier modes. The X axis points in the streamwise direction and $x \in [0, 1000]$, while the Y axis is perpendicular to the wall and $y \in [0, 60]$. The Z axis follows the right-hand rule and $z \in [-25, 25]$.

The simulation is periodic in the spanwise direction, and periodicity along the streamwise direction is assured by the introduction of a fringe region comprising positions $x_{fringe} \in [900, 1000]$. All variables are non-dimensionalised by the free-stream velocity U_∞ and displacement thickness δ_0^* at the intake position where $Re^* = U_\infty \delta_0^* / \nu = 300$, with ν being the kinematic viscosity of the fluid.

In order to produce isotropic turbulence at the free stream, a number of modes from the continuous branch of the Orr–Sommerfeld and Squire operators are forced in the fringe region, with a turbulence intensity of 3.0 % measured at root mean square level, in the same way of Sasaki *et al.* (2020), following Brandt *et al.* (2004). The resulting database is composed of 2000 snapshots of fully developed, statistically stationary velocity fluctuation fields around the Blasius base flow, computed with a constant time step of $\delta t = 10$. The domain is long enough to display the growth of streaks in the laminar upstream region, but ends before the development of turbulent spots, as seen in figure 13.

5.2.1. *Spectral POD and shifted SPOD*

Since the domain is periodic in Z, a Fourier decomposition can be performed in this direction and each wavenumber β can be analysed separately, making the velocity field

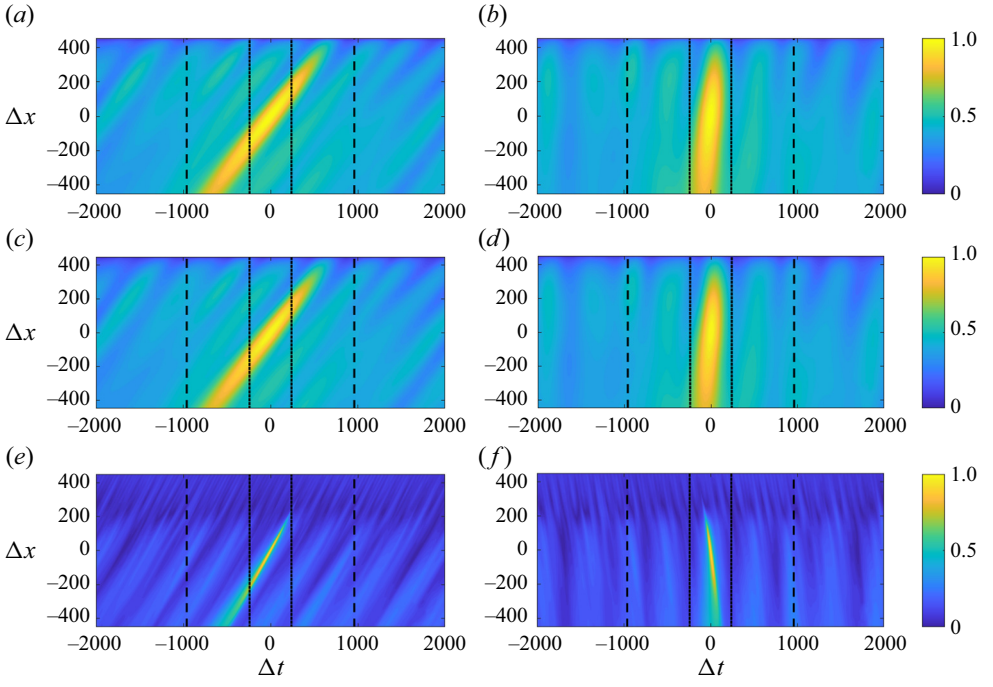

Figure 14. Space–time cross-correlation for $\beta = 0.377$ of the u velocity component at different distances from the wall. Results are shown for (a,b) $y = 0.01$; (c,d) $y = 1$; (e,f) $y = 6$. (a,c,d) Non-shifted field. (b,d,f) Shifted field. Dashed line: $N_{FFT} = 192$; dotted line: $N_{FFT} = 48$.

effectively two dimensional for each β. Following the definitions of § 2, the state vector $\boldsymbol{q}$ is defined according to (2.4) and the inner-product weight matrix $\boldsymbol{W}$ is designed to account for the grid quadrature. Spectral POD modes are computed for $x \in [0, 900]$, excluding the fringe zone. We employ the same windowing function from (5.7) which allows an overlap of 75 % between blocks.

In order to better study the effects of window sizing, we consider two cases with a time series division in $N_{FFT_1} = 48$ and $N_{FFT_2} = 192$ snapshots per block, leading to, respectively, $N_{b_1} = 330$ and $N_{b_2} = 38$ blocks with the standard method and $N_{b_1} = 310$ and $N_{b_2} = 36$ with the shifted one. As the streaky structures involved in the bypass transition have very low characteristic frequency and slow dynamics (Nogueira *et al.* 2019; Pickering *et al.* 2020; Nidhan *et al.* 2020), we focus the analysis on SPOD modes at the lowest non-zero frequency in case 1, $\omega = 0.0131$.

Following the steps described in § 4.2, for the shifted SPOD algorithm, (i) we choose to compute time lags with respect to the streamwise position $x_p = 450$, the farthest possible from the influence of the fringe region. (ii) In figure 14(a,c,e) we plot the space–time correlations for the streamwise component u at different distances from the wall. (iii) A constant shifting velocity $U_k = 0.75$ (4.1) was fixed for all points. In this case, the shifting velocity does not match the free-stream velocity $U_\infty = 1$. This was carefully set to align approximately the cross-correlations of points inside the boundary layer, as shown in figure 14(b,d,f). (iv) The alignment of peaks generated by the shift allows the bulk of correlation, that required a window of size $N_{FFT} = 192$, to be captured in a much smaller window of $N_{FFT} = 48$.

Results for the most energetic spanwise wavenumber $\beta = 0.377$ at frequency $\omega = 0.0131$ are displayed in figure 15. Figure 15(*a*,*d*) displays eigenvalues as a fraction of total energy. With both methods, the first mode dominates the flow dynamics. At $N_{FFT} = 48$, the first standard SPOD mode accounts for 47.3 % of the energy, while the corresponding shifted SPOD mode captures 77.4 %. At $N_{FFT} = 192$, these values correspond to 64.6 % and 82.9 %, respectively. In both cases, the shifted SPOD is able to capture more energy in the first mode.

We can quantify the similarity between modes computed with different windows sizes by calculating alignment coefficients

$$\mu_{i,j}(\omega) = \frac{|\langle \hat{\boldsymbol{\psi}}_i(\omega), \hat{\boldsymbol{\psi}}_j(\omega) \rangle|}{\|\hat{\boldsymbol{\psi}}_i(\omega)\| \cdot \|\hat{\boldsymbol{\psi}}_j(\omega)\|} \tag{5.9}$$

from which we get $\mu_{48,192} = 0.23$ for standard SPOD and $\mu_{48,192} = 0.88$ for shifted SPOD. The higher alignment between modes computed with the shifted algorithm puts in evidence its lower sensitivity with respect to the window size parameter.

5.2.2. *Comparison with resolvent analysis*

With the purpose of providing a deeper insight of the intrinsic dynamics of the boundary layer system, global resolvent modes, computed according to the method presented in Kaplan *et al.* (2021) and Abreu *et al.* (2021), are compared with the available SPOD modes. The governing Navier–Stokes equations are linearised around a Blasius profile base flow and cast in an input–output form, as described in § 3. Even though this is a nonlinear system, it is presumed that, when the resolvent gains display an expressive separation in magnitude, the first SPOD and resolvent response modes are similar regardless of the nonlinear forcing statistics (Beneddine *et al.* 2016). This effect has already been observed in turbulent flows (Schmidt *et al.* 2018; Cavalieri *et al.* 2019; Lesshaft *et al.* 2019; Abreu *et al.* 2020*b*).

The global resolvent computational domain was defined similarly to the LES, with the same domain size discretised with a 512×121 ($X \times Y$) grid. We introduce a fringe zone in $x_{fringe} \in [900, 1000]$ where fluctuations are damped and the base flow field is artificially treated to enforce the periodicity in X (figure 16). Homogeneous boundary conditions for fluctuations are set at the lower and upper domain limits. Derivatives are approximated by a fourth-order finite differences scheme in X and Chebyshev polynomials in Y.

As in LES, all variables are non-dimensionalised by the displacement thickness δ^* and free-stream velocity $U_\infty = 1$ at the intake, where $Re^* = 300$. Periodicity in the spanwise direction and stationarity imply the normal mode ansatz

$$\tilde{\boldsymbol{q}}(x, y, z, t) = \hat{\boldsymbol{q}}(x, y) \exp[\mathrm{i}(\beta z - \omega t)], \tag{5.10}$$

where the state vector $\boldsymbol{q} = [u, v, w, p]^{\mathrm{T}}$ contains the velocity components and the pressure stacked. The weight matrices $\boldsymbol{W}_y$ and $\boldsymbol{W}_f$ were set to account for the domain quadrature and the operator $\boldsymbol{B}$ restricts the forcing application to the space outside the fringe zone. The observation operator $\boldsymbol{H}$ removes the pressure component from the output, as the flow is incompressible and only the velocity field is analysed. Even though the state $\boldsymbol{q}$ contains points in the fringe, the resolvent operator gains only consider points outside of it, by a proper definition of $\boldsymbol{H}$.

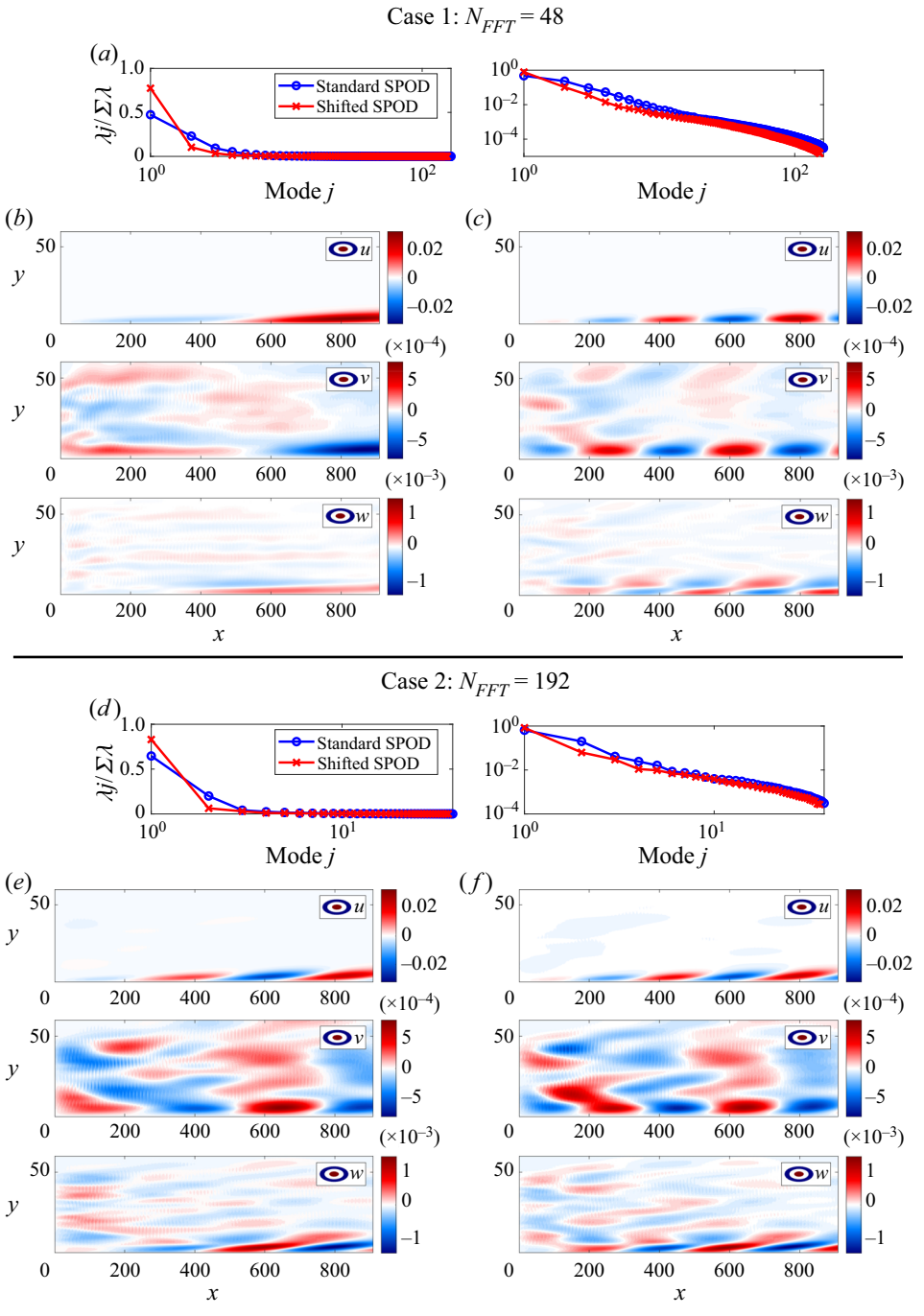

Figure 15. Results using a window of size $N_{FFT} = 48$ and $N_{FFT} = 192$ at $\beta = 0.377$, $\omega = 0.0131$. (*a*,*d*) Eigenvalues normalised by total energy. (*a*,*d*) Eigenvalues normalised by total energy. (*b*,*c*,*e*,*f*) Real part of the leading mode. (*b*,*e*) Standard SPOD. (*c*,*f*) Shifted SPOD.

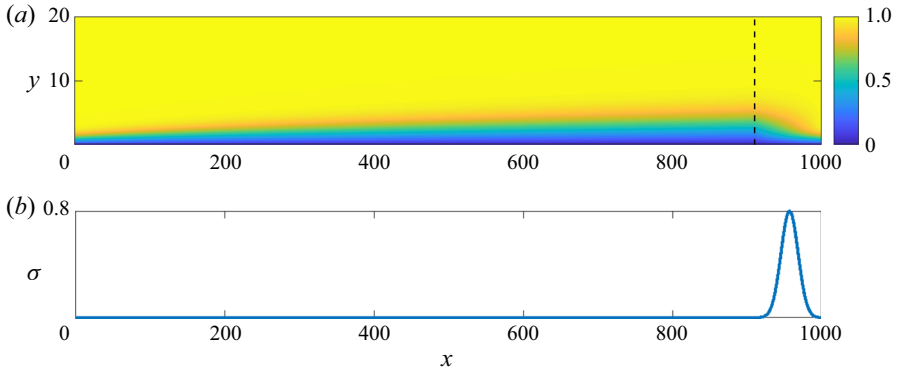

Figure 16. (*a*) Blasius mean velocity field (U component). The dashed line indicates the beginning of the fringe region. (*b*) Damping factor. The maximum of σ matches the value used in the LES.

Due to the significant size of matrices involved, the eigenproblem

$$\left.\begin{aligned} \boldsymbol{R}^H\boldsymbol{R}\boldsymbol{V} &= \boldsymbol{V}\boldsymbol{\Sigma}^2, \\ \boldsymbol{U} &= \boldsymbol{R}\boldsymbol{V}\boldsymbol{\Sigma}^{-1}, \end{aligned}\right\} \tag{5.11}$$

which calculates resolvent modes and gains is solved using sparse matrices via a lower-and-upper decomposition and 50 iterations of the Arnoldi method (Martini *et al.* 2021), without explicitly inverting $\boldsymbol{L}$. The details of this method are described in Kaplan *et al.* (2021). Results of the global resolvent analysis for the same $\beta = 0.377$ and $\omega = 0.0131$ as in the LES are displayed in figure 17. Figures 18 and 19 show the comparison between the reconstructed three-dimensional resolvent mode and the previously studied SPOD modes.

Figure 17(*a*) shows that the leading gain is sufficiently separated from the rest and, thus, the corresponding mode can be used as a comparison with the SPOD. Besides that, we observe in figure 17(*b*,*c*) that the leading response and forcing resolvent modes demonstrate the mechanism described in the lift-up effect: a forcing perpendicular to the streamwise direction, with a small f_x forcing component and larger f_y and f_z, generating a growing response primarily in the u velocity component. Such results are consistent with the earlier calculations by Monokrousos *et al.* (2010). From figure 18 it is clear that this dynamic generates intercalating regions of alternating streamwise velocity and counter-rotating streamwise vortices. When the vorticity transports matter downwards to the boundary layer, a positive streak is created, while the opposite occurs when matter is forced upwards.

For case 2, cross-sections of shifted and non-shifted SPOD modes are almost identical and match the dynamics of the most amplified linearised response. However, the same is not true for case 1, suggesting that streak skewness is an attribute sensitive to window size.

Other discrepancies are clear in figure 19. While the resolvent response and shifted modes feature aligned elongated structures, displaying the characteristic deviation caused by the phase velocity ω/β, the non-shifted mode in case 1 has an opposite trend. Since phase velocity is not affected by the windowing, we conclude that this is a convergence issue of the standard SPOD, corrected by the proposed temporal shift operation.

A growth of longitudinal vortices along the streamwise direction is perceived in the SPOD modes (magnitudes of v and w components in figure 15). This feature is predicted

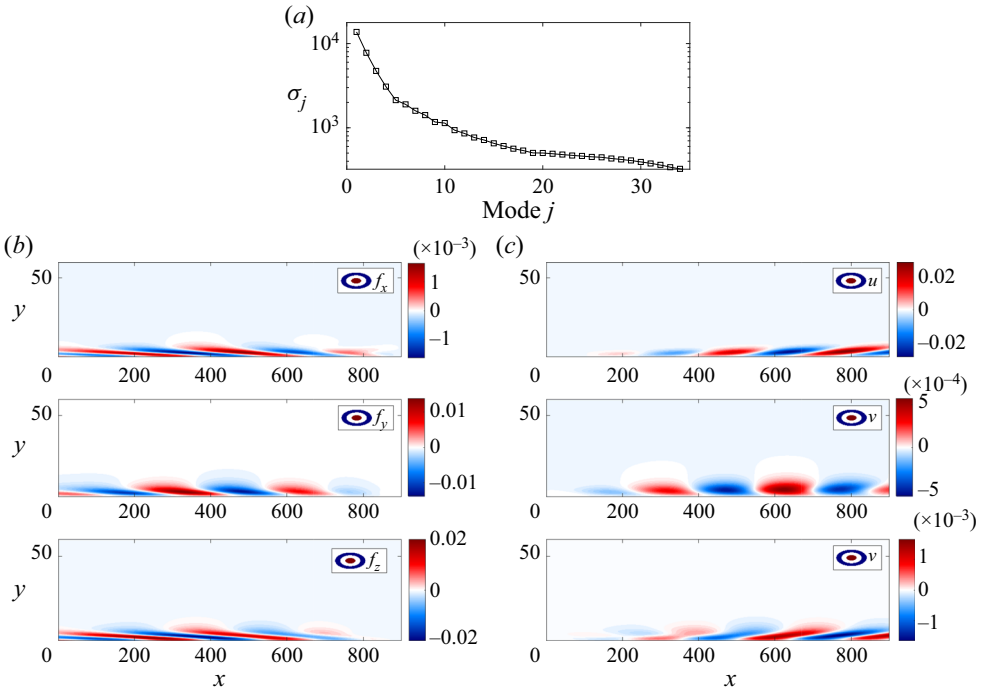

Figure 17. (*a*) Resolvent gains. (*b*) Real part of the leading forcing mode. (*c*) Real part of the leading response mode.

by the resolvent analysis, as seen in figure 17 and constitutes a different behaviour from that caused by the transient growth, where vortices decay in x while streaks grow (Andersson, Berggren & Henningson 1999; Luchini 2000). These results imply that the free-stream turbulence provides a continuous forcing to the streamwise vortices, which may be understood as projecting onto the forcing resolvent mode of figure 17(*b*) and leading to streamwise vortices and streaks that grow in x.

In a further analysis, focusing on case 2 ($N_{FFT} = 192$), the absolute value of each of the mode components are plotted for the position $x = 700$. In figure 20(*a*) the free-stream induced perturbations captured by SPOD modes are successful in matching the streamwise component of the optimal linearised response predicted by the resolvent operator and the overall form of the transverse components, of much smaller magnitude and, thus, more difficult to converge, is consistent. This fact corroborates the assumption concerning the similarity between SPOD and resolvent modes for large gain/energy separation, as is the case. It is also noted that leading shifted and non-shifted SPOD modes are practically identical at this streamwise position, a characteristic well depicted in figure 18. To evaluate the differences between them, a look into the subsequent mode is necessary (figure 20*b*). For the second mode, the agreement between SPOD and resolvent modes is not as close. Nevertheless, the shifted mode better matches the two-peak form and the maximum magnitude position of the linearised streamwise component.

To determine the statistical convergence of analysed modes, we apply the test employed in Abreu *et al.* (2020*b*) and compute SPOD modes considering two equal parts of the original database, each comprising 50 % of the total number of snapshots. Modes from part 1 are projected into modes from part 2 and alignment coefficients, defined in (5.9),

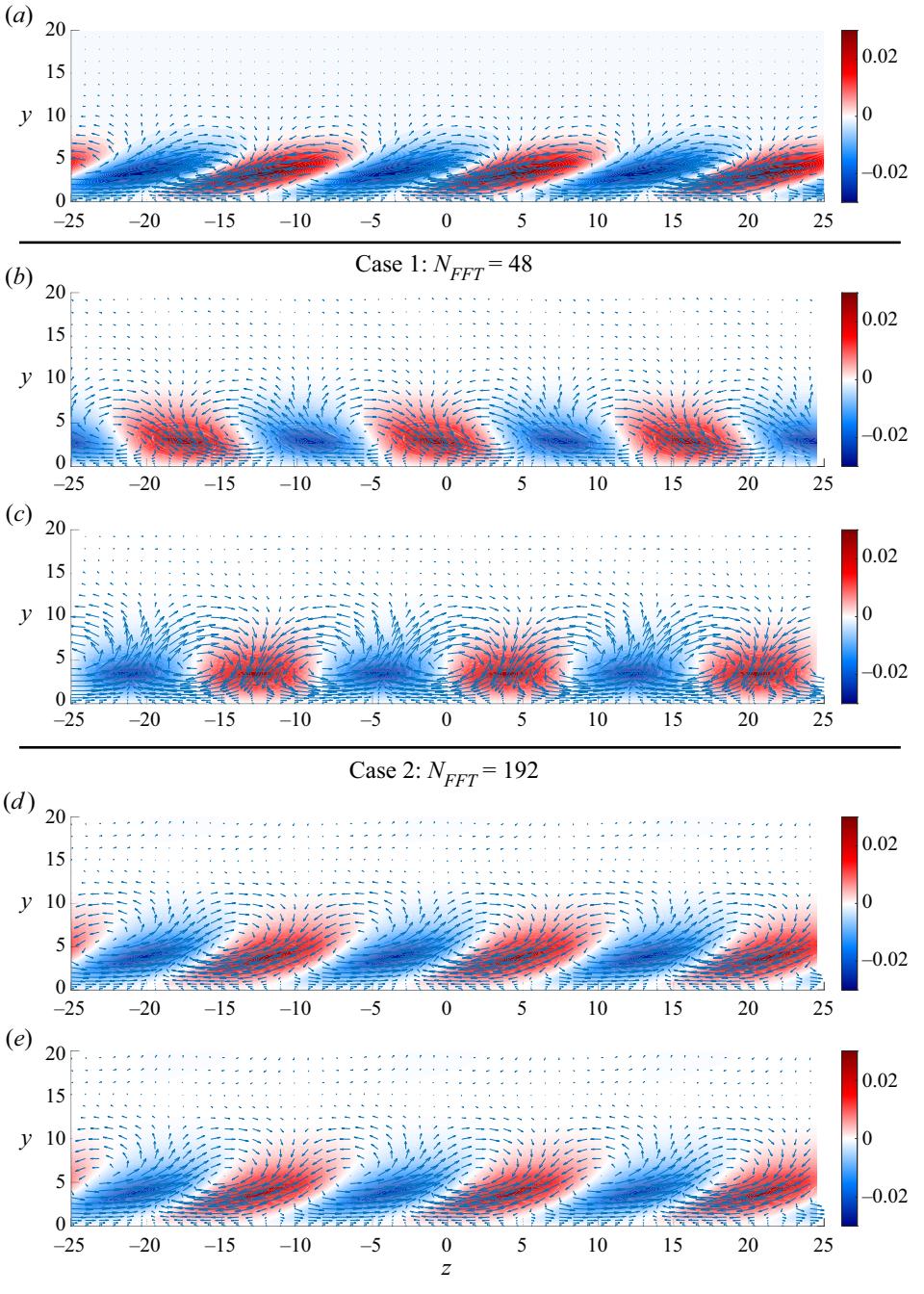

Figure 18. Section $x = 700$ of the reconstructed modes. Legend: (colours) u velocity component; (→) perpendicular velocity component. (*a*) Resolvent response. (*b*,*d*) Standard SPOD. (*c*,*e*) Shifted SPOD.

are calculated. For a given mode, a correlation close to 1 implies that the correspondent mode computed from the complete database is statistically converged. Results of this analysis (table 1) show that all modes achieve alignment coefficients higher than 90 %. This, in turn, indicates that discrepancies observed between shifted and non-shifted SPOD

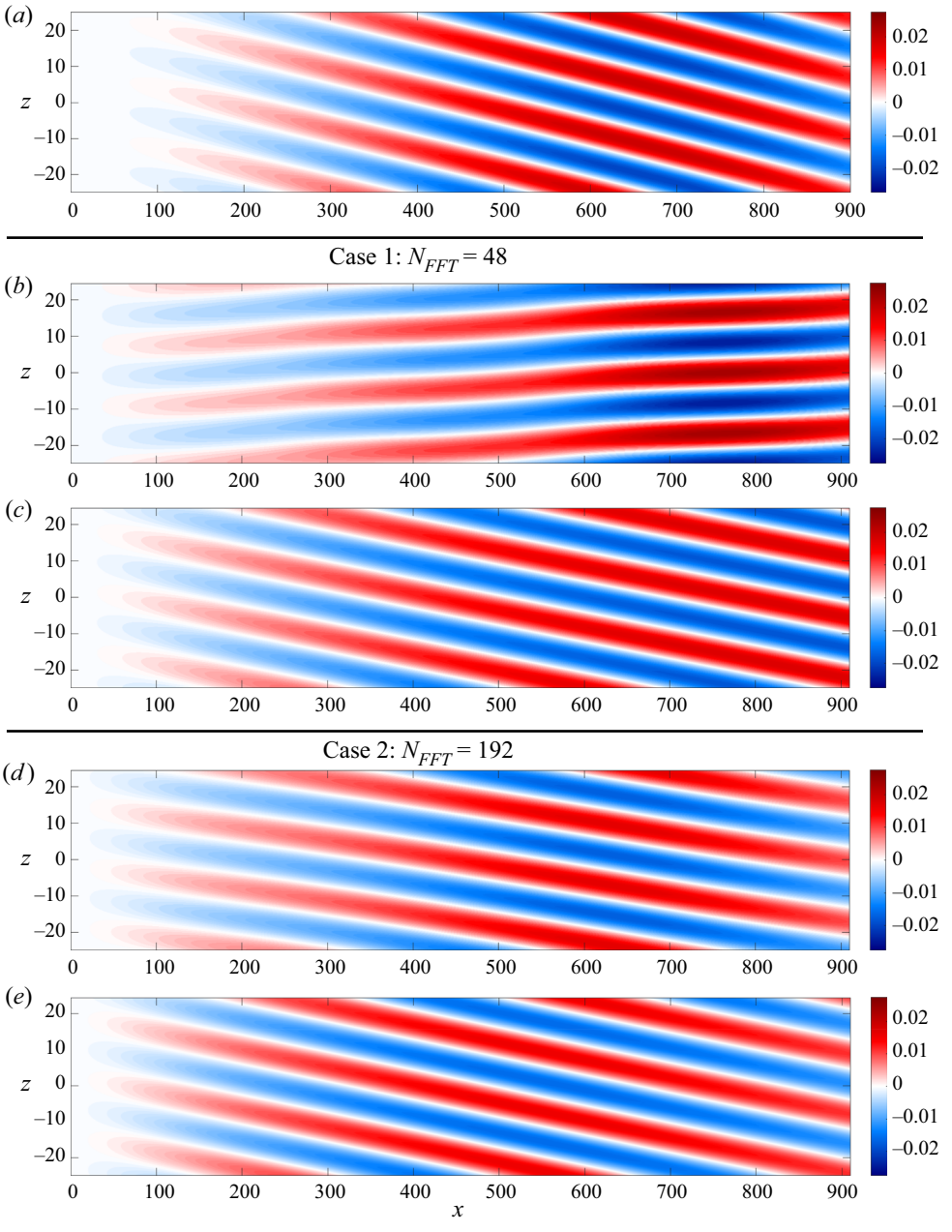

Figure 19. Section $y = 2$ of the reconstructed modes, inside the boundary layer. Legend: (colours) u velocity component. (a) Resolvent response. (b,d) Standard SPOD. (c,e) Shifted SPOD.

modes are not due to poor statistical significance, but rather to a reduction of bias caused by the temporal shift operation.

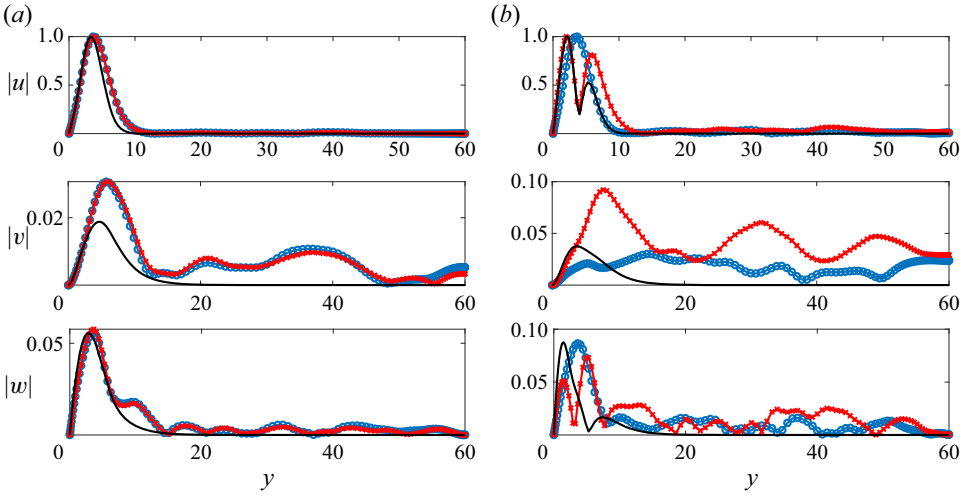

Figure 20. Normalised fluctuations at position $x = 700$ for case 2. (*a*) Mode 1. (*b*) Mode 2. Legend: (−) optimal linearised response (resolvent); (○, blue) standard SPOD; (×, red) shifted SPOD.

	Mode 1	Mode 2
Standard SPOD	0.9637	0.9390
Shifted SPOD	0.9842	0.9039

Table 1. Alignment coefficients at $N_{FFT} = 192$, $\omega = 0.0131$ and $\beta = 0.377$.

6. Conclusions

In the present study we explore the effect of estimation parameters (number of blocks and number of snapshots per block) on the convergence of SPOD, associated with the Welch method for spectral estimation. A convergence analysis is performed for a model linear complex Ginzburg–Landau system, forced with spatially uncorrelated signals, by measuring the estimation errors between numerical SPOD modes and resolvent response modes.

Estimation errors in SPOD are found to be related to the spectral window length, normalised by the domain size and characteristic velocity. As seen in figures 2 and 3, two main phenomena affect the convergence of the SPOD method. For shorter windows, with a duration comparable or lower than the flow-through time in the domain of interest, we average over a larger number of Welch blocks that are not sufficiently long to capture the space–time correlation in the system, which follows an advection velocity. This yields smooth albeit biased SPOD modes, meaning results are precise but not accurate. Inversely, for larger windows, we have fewer averaging blocks. This penalises precision as SPOD modes are contaminated with noise, due to residual variance.

An extension to the SPOD algorithm by means of a temporal data shift is proposed. By aligning cross-correlations between points inside each block, the new approach in shown to minimise the bias of SPOD modes computed with short window sizes, as seen in figure 5. This allows for better overall convergence as the SPOD can be computed with more blocks for a given time series. This is an important feature when dealing with large simulations that often count with a limited number of snapshots. Furthermore, when comparing the

standard and shifted SPODs in a fixed-block framework of constant variance (figure 7), shifted modes always display smaller estimation errors, achieving an order of magnitude difference for smaller windows.

In order to demonstrate the pertinence of the proposed method in fluid dynamics problems, we apply the temporal shift to an LES of a boundary layer subject to bypass transition, and SPOD modes are compared with global resolvent modes. Even though equivalence is no longer guaranteed for nonlinear systems (coloured forcing), SPOD and resolvent modes are still similar when gain separation is large, as in the boundary layer case.

Results show that the shifted SPOD, for the same estimation parameters, captures more energy in the leading mode when compared with the standard method. In SPOD modes a spatial growth of streamwise vortices is observed, a feature also present in the resolvent analysis but absent from spatial transient growth analysis (Andersson *et al.* 1999; Luchini 2000). This implies that the free-stream turbulence continuously 'forces' streamwise vortices, leading to additional spatial growth of disturbances. When a single streamwise section is compared, shifted and non-shifted SPOD leading modes are very close and match the u component of the optimal linear response (leading resolvent mode). Discrepancies arise when the second mode is looked upon. The shifted mode is closer to the u component in the linear response. A further statistical convergence test indicates these changes are not due to lack of statistical significance, but rather to a reduction of bias caused by the shifting operation.

Acknowledgements. The scripts necessary to run the Ginzburg–Landau cases and SPOD computations are available in a public GIT repository at https://github.com/DiegoCPB/Shifted-SPOD.

Funding. This work is financially supported by Fundação de Amparo à Pesquisa do Estado de São Paulo, FAPESP, under grants nos. 2019/27655-3 and 2020/14200-5 for D.C.P.B.

Declaration of interests. The authors report no conflict of interest.

Author ORCIDs.
Diego C.P. Blanco https://orcid.org/0000-0003-2475-8986;
Eduardo Martini https://orcid.org/0000-0002-3144-5702;
Kenzo Sasaki https://orcid.org/0000-0002-3347-4996;
André V.G. Cavalieri https://orcid.org/0000-0003-4283-0232.

Appendix A. Relationship between SPOD and resolvent analysis for an arbitrary inner-product norm

Considering the inner products

$$\langle \hat{y}_1, \hat{y}_2 \rangle_{W_y} = \hat{y}_1^H W_y \hat{y}_2, \tag{A1}$$

$$\left\langle \hat{f}_1, \hat{f}_2 \right\rangle_{W_f} = \hat{f}_1^H W_f \hat{f}_2, \tag{A2}$$

and the resolvent operator $\boldsymbol{R}$, we compute response modes $\boldsymbol{U}$, forcing modes $\boldsymbol{V}$ and gains $\boldsymbol{\Sigma}$ via the SVD,

$$\tilde{y} = W_y^{1/2} \hat{y}, \quad \tilde{f} = W_f^{1/2} \hat{f}, \tag{A3a,b}$$

$$\tilde{y} = \tilde{\boldsymbol{R}} \tilde{f} \implies \tilde{\boldsymbol{R}} = W_y^{1/2} \boldsymbol{R} W_f^{-1/2}, \tag{A4}$$

$$\tilde{\boldsymbol{R}}\tilde{\boldsymbol{V}} = \tilde{\boldsymbol{U}}\boldsymbol{\Sigma} \implies \boldsymbol{R}\boldsymbol{W}_f^{-1/2}\tilde{\boldsymbol{V}} = \boldsymbol{W}_y^{-1/2}\tilde{\boldsymbol{U}}\boldsymbol{\Sigma}, \tag{A5}$$

$$\boldsymbol{U} = \boldsymbol{W}_y^{-1/2}\tilde{\boldsymbol{U}}, \quad \boldsymbol{V} = \boldsymbol{W}_f^{-1/2}\tilde{\boldsymbol{V}}. \tag{A6a,b}$$

We assume that

$$\boldsymbol{C}_\omega = \mathcal{E}\left(\hat{\boldsymbol{y}}\hat{\boldsymbol{y}}^H\boldsymbol{W}_y\right), \tag{A7}$$

$$\boldsymbol{F}_\omega = \mathcal{E}\left(\hat{\boldsymbol{f}}\hat{\boldsymbol{f}}^H\boldsymbol{W}_f\right), \tag{A8}$$

which imply from the resolvent framework (3.3),

$$\boldsymbol{C}_\omega = \boldsymbol{R}\boldsymbol{F}_\omega\boldsymbol{W}_f^{-1}\boldsymbol{R}^H\boldsymbol{W}_y. \tag{A9}$$

If forcing terms are perfectly uncorrelated, $\boldsymbol{F}_\omega = \boldsymbol{I}$ and the expression can be reduced to

$$\begin{aligned}\boldsymbol{C}_\omega &= \boldsymbol{R}\boldsymbol{W}_f^{-1}\boldsymbol{R}^H\boldsymbol{W}_y = \boldsymbol{W}_y^{-1/2}\tilde{\boldsymbol{R}}\tilde{\boldsymbol{R}}^H\boldsymbol{W}_y^{1/2} \\ &= \boldsymbol{W}_y^{-1/2}\tilde{\boldsymbol{U}}\boldsymbol{\Sigma}^2\tilde{\boldsymbol{U}}^{-1}\boldsymbol{W}_y^{1/2}\end{aligned} \tag{A10}$$

and, thus, substituting (A6a,b), we have

$$\boldsymbol{C}_\omega = \boldsymbol{U}\boldsymbol{\Sigma}^2\boldsymbol{U}^{-1}, \tag{A11}$$

as in (3.8).

Appendix B. On the convergence of the shifted spectral estimation

Given two bounded, stationary signals $a(t)$ and $b(t)$, the Fourier transforms of the windowed signals within each Welch block are given by

$$\hat{a}_h(\omega) = \mathcal{F}\{h(t)a(t)\} = \frac{1}{T}\int_{t_0}^{t_0+T} h(t)a(t)\mathrm{e}^{\mathrm{i}\omega t}\,\mathrm{d}t, \tag{B1}$$

$$\hat{b}_h(\omega,\tau) = \mathcal{F}\{h(t)b(t+\tau)\} = \frac{1}{T}\int_{t_0}^{t_0+T} h(t)b(t+\tau)\mathrm{e}^{\mathrm{i}\omega t}\,\mathrm{d}t, \tag{B2}$$

where t_0 denotes the initial time for each block, T the block duration, $h(t)$ the windowing function and τ the time shift.

Following the properties of the Fourier transform, a time shift τ generates a phase lag of $\exp(\mathrm{i}\omega\tau)$. Thus, we write the corrected cross-periodogram as

$$S(\omega,\tau) = \hat{a}_h(\omega)\hat{b}_h(\omega,\tau)\mathrm{e}^{-\mathrm{i}\omega\tau}. \tag{B3}$$

In the limit where $T \to \infty$, we have

$$\lim_{T\to\infty} h(t) = 1, \tag{B4}$$

$$\lim_{T\to\infty} \hat{a}_h(\omega) = \mathcal{F}\{a(t)\} = \hat{a}(\omega), \tag{B5}$$

$$\lim_{T\to\infty} \hat{b}_h(\omega,\tau) = \mathcal{F}\{b(t+\tau)\} = \hat{b}(\omega)\mathrm{e}^{\mathrm{i}\omega\tau}, \tag{B6}$$

which leads to the true cross-periodogram

$$\lim_{T\to\infty} S(\omega,\tau) = \hat{a}(\omega)\hat{b}(\omega) \tag{B7}$$

and demonstrates that the procedure converges asymptotically for an arbitrary time shift and frequency. In that sense, shifted and non-shifted spectral estimations must return the same results for a large enough window size.

References

Abreu, L.I., Cavalieri, A.V.G., Schlatter, P., Vinuesa, R. & Henningson, D.S. 2020*a* Resolvent modelling of near-wall coherent structures in turbulent channel flow. *Intl J. Heat Fluid Flow* **85**, 108662.

Abreu, L.I., Cavalieri, A.V.G., Schlatter, P., Vinuesa, R. & Henningson, D.S. 2020*b* Spectral proper orthogonal decomposition and resolvent analysis of near-wall coherent structures in turbulent pipe flows. *J. Fluid Mech.* **900**, A11.

Abreu, L.I., Tanarro, A., Cavalieri, A.V.G., Schlatter, P., Vinuesa, R., Hanifi, A. & Henningson, D.S. 2021 Spanwise-coherent hydrodynamic waves around flat plates and airfoils. *J. Fluid Mech.* **927**, A1.

Andersson, P., Berggren, M. & Henningson, D.S. 1999 Optimal disturbances and bypass transition in boundary layers. *Phys. Fluids* **11** (1), 134–150.

Aranson, I.S. & Kramer, L. 2002 The world of the complex Ginzburg–Landau equation. *Rev. Mod. Phys.* **74**, 99–143.

Araya, D.B., Colonius, T. & Dabiri, J.O. 2017 Transition to bluff-body dynamics in the wake of vertical-axis wind turbines. *J. Fluid Mech.* **813**, 346–381.

Arndt, R.E.A., Long, D.F. & Glauser, M.N. 1997 The proper orthogonal decomposition of pressure fluctuations surrounding a turbulent jet. *J. Fluid Mech.* **340**, 1–33.

Aubry, N. 1991 On the hidden beauty of the proper orthogonal decomposition. *Theor. Comput. Fluid Dyn.* **2** (5), 339–352.

Bagheri, S., Henningson, D.S., Hœpffner, J. & Schmid, P.J. 2009 Input–output analysis and control design applied to a linear model of spatially developing flows. *Appl. Mech. Rev.* **62** (2), 020803.

Beneddine, S., Sipp, D., Arnault, A., Dandois, J. & Lesshafft, L. 2016 Conditions for validity of mean flow stability analysis. *J. Fluid Mech.* **798**, 485–504.

Berkooz, G., Holmes, P. & Lumley, J.L. 1993 The proper orthogonal decomposition in the analysis of turbulent flows. *Annu. Rev. Fluid Mech.* **25**, 539–575.

Bonnet, J.P., *et al.* 1998 Collaborative testing of eddy structure identification methods in free turbulent shear flows. *Exp. Fluids* **25** (3), 197–225.

Brandt, L. 2014 The lift-up effect: the linear mechanism behind transition and turbulence in shear flows. *Eur. J. Mech. B/Fluids* **47**, 80–96.

Brandt, L., Schlatter, P. & Henningson, D.S. 2004 Transition in boundary layers subject to free-stream turbulence. *J. Fluid Mech.* **517**, 167–198.

Cavalieri, A.V.G., Jordan, P. & Lesshafft, L. 2019 Wave-packet models for jet dynamics and sound radiation. *Appl. Mech. Rev.* **71** (2), 020802.

Chevalier, M., Lundbladh, A. & Henningson, D.S. 2007 Simson – a pseudo-spectral solver for incompressible boundary layer flow. Tech. Rep. TRITA-MEK.

Citriniti, J.H. & George, W.K. 2000 Reconstruction of the global velocity field in the axisymmetric mixing layer utilizing the proper orthogonal decomposition. *J. Fluid Mech.* **418**, 137–166.

Delville, J., Ukeiley, L., Cordier, L., Bonnet, J.P. & Glauser, M. 1999 Examination of large-scale structures in a turbulent plane mixing layer. Part 1. Proper orthogonal decomposition. *J. Fluid Mech.* **391**, 91–122.

Ellingsen, T. & Palm, E. 1975 Stability of linear flow. *Phys. Fluids* **18** (4), 487–488.

Glauser, M.N. & George, W. 1987 Orthogonal decomposition of the axisymmetric jet mixing layer including azimuthal dependence. In *Advances in Turbulence* (ed. F. Durst *et al.*), pp. 357–366. Springer.

Gudmundsson, K. & Colonius, T. 2011 Instability wave models for the near-field fluctuations of turbulent jets. *J. Fluid Mech.* **689**, 97–128.

He, X., Fang, Z., Rigas, G. & Vahdati, M. 2021 Spectral proper orthogonal decomposition of compressor tip leakage flow. *Phys. Fluids* **33** (10), 105105.

He, G., Jin, G. & Yang, Y. 2017 Space–time correlations and dynamic coupling in turbulent flows. *Annu. Rev. Fluid Mech.* **49** (1), 51–70.

Hellström, L.H.O. & Smits, A.J. 2014 The energetic motions in turbulent pipe flow. *Phys. Fluids* **26** (12), 125102.

Huerre, P. & Monkewitz, P.A. 1990 Local and global instabilities in spatially developing flows. *Annu. Rev. Fluid Mech.* **22** (1), 473–537.

Iqbal, M.O. & Thomas, F.O. 2007 Coherent structure in a turbulent jet via a vector implementation of the proper orthogonal decomposition. *J. Fluid Mech.* **571**, 281–326.

Jaunet, V., Jordan, P. & Cavalieri, A.V.G. 2017 Two-point coherence of wave packets in turbulent jets. *Phys. Rev. Fluids* **2**, 024604.

Jovanović, M.R. & Bamieh, B. 2005 Componentwise energy amplification in channel flows. *J. Fluid Mech.* **534**, 145–183.

JUNG, D., GAMARD, S. & GEORGE, W.K. 2004 Downstream evolution of the most energetic modes in a turbulent axisymmetric jet at high Reynolds number. Part 1. The near-field region. *J. Fluid Mech.* **514**, 173–204.

KAPLAN, O., JORDAN, P., CAVALIERI, A.V.G. & BRÈS, G.A. 2021 Nozzle dynamics and wavepackets in turbulent jets. *J. Fluid Mech.* **923**, A22.

LESSHAFT, L., SEMERARO, O., JAUNET, V., CAVALIERI, A.V.G. & JORDAN, P. 2019 Resolvent-based modeling of coherent wave packets in a turbulent jet. *Phys. Rev. Fluids* **4**, 063901.

LI, X.-B. , CHEN, G., LIANG, X.-F., LIU, D.-R. & XIONG, X.-H. 2021 Research on spectral estimation parameters for application of spectral proper orthogonal decomposition in train wake flows. *Phys. Fluids* **33** (12), 125103.

LUCHINI, P. 2000 Reynolds-number-independent instability of the boundary layer over a flat surface: optimal perturbations. *J. Fluid Mech.* **404**, 289–309.

LUGRIN, M., BENEDDINE, S., LECLERCQ, C., GARNIER, E. & BUR, R. 2021 Transition scenario in hypersonic axisymmetrical compression ramp flow. *J. Fluid Mech.* **907**, A6.

LUMLEY, J.L. 1967 The structure of inhomogeneous turbulent flows. In *Atmospheric Turbulence and Radio Wave Propagation* (ed. A.M. Yaglom & V.I. Tatarski). Nauka.

LUMLEY, J.L. 1970 *Stochastic Tools in Turbulence*. Academic Press.

MARTINI, E., CAVALIERI, A.V.G., JORDAN, P. & LESSHAFFT, L. 2020 Accurate frequency domain identification of ODEs with arbitrary signals. arXiv:1907.04787.

MARTINI, E., RODRÍGUEZ, D., TOWNE, A. & CAVALIERI, A.V.G. 2021 Efficient computation of global resolvent modes. *J. Fluid Mech.* **919**, A3.

MATSUBARA, M. & ALFREDSSON, P.H. 2001 Disturbance growth in boundary layers subjected to free-stream turbulence. *J. Fluid Mech.* **430**, 149–168.

MCKEON, B.J. & SHARMA, A.S. 2010 A critical-layer framework for turbulent pipe flow. *J. Fluid Mech.* **658**, 336–382.

MONOKROUSOS, A., ÅKERVIK, E., BRANDT, L. & HENNINGSON, D. 2010 Global three-dimensional optimal disturbances in the Blasius boundary-layer flow using time-steppers. *J. Fluid Mech.* **650**, 181–214.

NIDHAN, S., CHONGSIRIPINYO, K., SCHMIDT, O.T. & SARKAR, S. 2020 Spectral proper orthogonal decomposition analysis of the turbulent wake of a disk at $Re = 50\,000$. *Phys. Rev. Fluids* **5**, 124606.

NOACK, B.R., AFANASIEV, K., MORZYŃSKI, M., TADMOR, G. & THIELE, F. 2003 A hierarchy of low-dimensional models for the transient and post-transient cylinder wake. *J. Fluid Mech.* **497**, 335–363.

NOGUEIRA, P.A.S., CAVALIERI, A.V.G., JORDAN, P. & JAUNET, V. 2019 Large-scale streaky structures in turbulent jets. *J. Fluid Mech.* **873**, 211–237.

PICARD, C. & DELVILLE, J. 2000 Pressure velocity coupling in a subsonic round jet. *Intl J. Heat Fluid Flow* **21** (3), 359–364.

PICKERING, E., RIGAS, G., NOGUEIRA, P.A.S., CAVALIERI, A.V.G., SCHMIDT, O.T. & COLONIUS, T. 2020 Lift-up, Kelvin–Helmholtz and Orr mechanisms in turbulent jets. *J. Fluid Mech.* **896**, A2.

RAVINDRAN, S.S. 2000 A reduced-order approach for optimal control of fluids using proper orthogonal decomposition. *Intl J. Numer. Meth. Fluids* **34** (5), 425–448.

REISS, J., SCHULZE, P., SESTERHENN, J. & MEHRMANN, V. 2018 The shifted proper orthogonal decomposition: a mode decomposition for multiple transport phenomena. *SIAM J. Sci. Comput.* **40** (3), A1322–A1344.

ROWLEY, C.W. & DAWNSON, S.T. 2017 Model reduction for flow analysis and control. *Annu. Rev. Fluid Mech.* **49** (1), 387–417.

SANO, A., ABREU, L.I., CAVALIERI, A.V.G. & WOLF, W.R. 2019 Trailing-edge noise from the scattering of spanwise-coherent structures. *Phys. Rev. Fluids* **4**, 094602.

SASAKI, K., MORRA, P., CAVALIERI, A.V.G., HANIFI, A. & HENNINGSON, D.S. 2020 On the role of actuation for the control of streaky structures in boundary layers. *J. Fluid Mech.* **883**, A34.

SCHMIDT, O.T. & COLONIUS, T. 2020 Guide to spectral proper orthogonal decomposition. *AIAA J.* **58** (3), 1023–1033.

SCHMIDT, O.T. & TOWNE, A. 2019 An efficient streaming algorithm for spectral proper orthogonal decomposition. *Comput. Phys. Commun.* **237**, 98–109.

SCHMIDT, O.T., TOWNE, A., COLONIUS, T., CAVALIERI, A.V.G., JORDAN, P. & BRÈS, G.A. 2017 Wavepackets and trapped acoustic modes in a turbulent jet: coherent structure eduction and global stability. *J. Fluid Mech.* **825**, 1153–1181.

SCHMIDT, O.T., TOWNE, A., RIGAS, G., COLONIUS, T. & BRES, G.A. 2018 Spectral analysis of jet turbulence. *J. Fluid Mech.* **855**, 953–982.

SIEBER, M., PASCHEREIT, C.O. & OBERLEITHNER, K. 2016 Spectral proper orthogonal decomposition. *J. Fluid Mech.* **792**, 798–828.

SIROVICH, L. 1987 Turbulence and the dynamics of coherent structures. Part I: coherent structures. *Q. Appl. Maths* **45** (3), 561–571.

TAIRA, K., HEMATI, M.S., BRUNTON, S.L., SUN, Y., DURAISAMY, K., BAGHERI, S., DAWSON, S.T.M. & YEH, C.-A. 2020 Modal analysis of fluid flows: applications and outlook. *AIAA J.* **58** (3), 998–1022.

TINNEY, C.E. & JORDAN, P. 2008 The near pressure field of co-axial subsonic jets. *J. Fluid Mech.* **611**, 175–204.

TOWNE, A., SCHMIDT, O.T. & COLONIUS, T. 2018 Spectral proper orthogonal decomposition and its relationship to dynamic mode decomposition and resolvent analysis. *J. Fluid Mech.* **847**, 821–867.

TUTKUN, M. & GEORGE, W.K. 2017 Lumley decomposition of turbulent boundary layer at high Reynolds numbers. *Phys. Fluids* **29** (2), 020707.

WELCH, P.D. 1967 The use of fast fourier transform for the estimation of power spectra: a method based on time averaging over short, modified periodograms. *IEEE Trans. Audio Electroacoust.* **15** (2), 70–73.

ZHANG, B., OOKA, R. & KIKUMOTO, H. 2021 Identification of three-dimensional flow features around a square-section building model via spectral proper orthogonal decomposition. *Phys. Fluids* **33** (3), 035151.